Journal Pre-proof

An alternative approach for robot localization inside pipes using RF spatial fadings

Carlos Rizzo, Teresa Seco, Jesús Espelosín, Francisco Lera, José Luis Villarroel

PII: S0921-8890(20)30542-X
DOI: https://doi.org/10.1016/j.robot.2020.103702
Reference: ROBOT 103702

To appear in: *Robotics and Autonomous Systems*

Received date : 30 April 2019
Revised date : 18 September 2020
Accepted date : 23 November 2020

Please cite this article as: C. Rizzo, T. Seco, J. Espelosín et al., An alternative approach for robot localization inside pipes using RF spatial fadings, *Robotics and Autonomous Systems* (2020), doi: https://doi.org/10.1016/j.robot.2020.103702.

An Alternative Approach for Robot Localization Inside Pipes using RF Spatial Fadings

Carlos Rizzo*[1], Teresa Seco*[2], Jesús Espelosín[2], Francisco Lera[3] and José Luis Villarroel[3]

***Abstract*—Accurate robot localization represents a challenge inside pipes due to the particular conditions that characterize this type of environment. Outdoor techniques (GPS in particular) do not work at all inside metal pipes, while traditional indoor localization methods based on camera or laser sensors do not perform well mainly due to a lack of external illumination and distinctive features along pipes. Moreover, humidity and slippery surfaces make wheel odometry unreliable. In this paper, we estimate the localization of a robot along a pipe with an alternative Radio Frequency (RF) approach. We first analyze wireless propagation in metallic pipes and propose a series of setups that allow us to obtain periodic RF spatial fadings (a sort of standing wave periodic pattern), together with the influence of the antenna position and orientation over these fadings. Subsequently, we propose a discrete RF odometry-like method, by means of counting the fadings while traversing them. The transversal fading analysis (number of antennas and cross-section position) makes it possible to increase the resolution of this method. Lastly, the model of the signal is used in a continuous approach serving as an RF map. The proposed localization methods outperform our previous contributions in terms of resolution, accuracy, reliability and robustness. Experimental results demonstrate the effectiveness of the RF-based strategy without the need for a previously known map of the scenario or any substantial modification of the existing infrastructure.**

***Keywords*-robotics; pipes; tunnels; propagation; RF fadings; localization; navigation; inspection; maintenance;**

I. INTRODUCTION

Pipe environments such as sewers, gas pipelines or dam drainpipes are exposed to structural damage over time. Inspection tasks are critical in order to detect and identify fissures, rusty areas, cracks or leakages that could have serious consequences for the safety of the infrastructure.

In recent years, robots have emerged as one of the best options for performing inspection tasks due to the harsh conditions of this type of environment: darkness, humidity and even physical limitations [1]. In this context, accurate robot localization is essential not only for identifying the position of any damage, but also for autonomous navigation. While identifying robots' position in the cross-section of pipes could be achieved using traditional techniques, localization along the longitudinal axis represents a challenge due to the fact that pipes' internal surfaces tend to be uniform (possibly without detectable features) and they are typically much longer than they are wide. Moreover, the aforementioned special nature of the environment makes the use of some common localization sensors unfeasible. This is the case of GPS sensor, for instance, that cannot be used in confined scenarios.

Fig. 1. Santa Ana dam drainpipe. Symmetric and smooth inner surface without distinguishable features.

In [2] the authors present a review of localization methods for small-diameter pipelines using PIG (Pipeline Inspection Gauge) technology. The localization methods are mainly based on the fusion of the information provided by Inertial Navigation System (INS) and odometers. The accumulated error is corrected in two ways: using Above Ground Markers (AGMs), which detect the passage of the PIG and provides it with GPS coordinates, and by means of detecting the pipeline junction with information from the inertial sensor ([3]–[5]). However, although PIG-based solutions are adequate for a wide range of small-diameter pipes, the drive systems of these devices, either by pressure difference between ends or by the use of a tether cable, makes them unfeasible for large-scale pipes. In addition, they are not self-contained and require installation of infrastructure (e.g. AGMs). At last, communication from inside the pipe is not always feasible.

In other studies, visual odometry-based methods are proposed to solve the localization inside pipes. The authors in [6] use monocular cameras, stereo cameras [7] or a monocular fisheye camera [8] with visual odometry algorithms for navigation in small cylindrical pipes. In [9], the authors present a localization system for sewers combining a known topological map with a manhole detection system, using RGB-D cameras and machine learning techniques. However, these algorithms based on cameras work properly if there are enough distin-

* The authors contributed equally. [1] Eurecat, Centre Tecnològic de Catalunya, Barcelona, Spain. [2] Instituto Tecnológico de Aragón, (ITAINNOVA), Zaragoza, Spain. [3] Robotics, Perception and Real-Time Group (RoPeRT), Aragón Institute for Engineering Research (I3A), University of Zaragoza, Spain. This work has been supported by the Spanish Ministry of Science, Innovation and Universities Project Robot navigation and deployment in challenging environments - Robochallenge (ref.DPI2016-76676-R-AEI/FEDER-UE) and by Aragon Government project DGA T45-17R. The authors would like to thank Mr. Felix Andreu from Confederación Hidrográfica del Ebro for his support in relation to the drainpipe of the Santa Ana dam in Castillonroy, Spain.

guishable surface features or irregularities, and tend to perform erratically in those cases of pipes that present symmetry and limited features (see Fig.1 as an example).

Regarding LiDAR-based systems, the unsuitability of using them to solve the localization in these environments is highlighted in [10] and [11], as the uncertainty in the longitudinal axis grows in the absence of structural features (e.g. a laser sensor only detects two parallel lines inside a long smooth pipe).

In real use-cases, the problems of vision and laser-based approaches are outlined, for example, in [12] and in [13] for the inspection of penstocks using Unmanned Aerial Vehicles (UAVs). Penstocks are large cylindrical pipes with two long non-parallel straight sections joint with an elbow. Having ruled out the use of vision in these environments, the authors propose the use of an Inertial Measurement Unit (IMU) and laser rangefinder sensors for localization. Nevertheless, the absence of detectable features makes longitudinal localization impossible if the junction between sections (acting as a wall at the end of the tunnel) is not in the range of the laser.

Other methods rely on wheel odometers for localization, but due to the high humidity and even the presence of fluids and mold, pipes tend to be slippery, making these methods inaccurate and unreliable for position estimation. In [14], the position of the robot along the pipe is obtained fusing the information provided by an IMU and a cable encoder which measures the length from the starting point to the tethered robot. Most of the time, these methods are unfeasible because of the length of the pipe or the type of robotic platform (e.g. drones).

Due to the aforementioned infeasibility of using sensors like GPS, cameras or lasers to determine the longitudinal localization of a robot inside a pipe, other technologies must be explored.

Recently-developed indoor positioning technologies rely on the use of Radio Frequency (RF) signal ([15], [16]). Ultra-Wideband (UWB), for example, is one of the most promising technologies for indoor localization, providing more accurate positioning and better performance than other RF technologies. Nevertheless, these RF-based indoor localization methods require prior collection of RF fingerprints of the scene to be compared afterwards with the online data (RF fingerprinting method) or at least three reference nodes placed with high precision in the infrastructure in the case of using trilateration algorithms to obtain the position [17]. Taking into account that inspection tasks are usually carried out during limited maintenance periods (e.g., a water pipe that needs to be emptied), the need for a commissioning step in order to place beacons or create an RF map makes these methods impractical. In [18], a robotic sensor network is proposed for localization in an underground plastic water pipeline. The simulated system consists of a mobile sensor node carried by the robot and multiple relay nodes placed aboveground (in a line parallel to the water pipeline), covering limited sections of the pipe. The position is obtained by fusing the RF signal measurements from the relay nodes and the velocity provided by an onboard IMU with an Extended Kalman Filter (EKF) algorithm. This solution is not suitable, however, for metallic pipes where the Faraday cage effect hinders communication between the inside and outside.

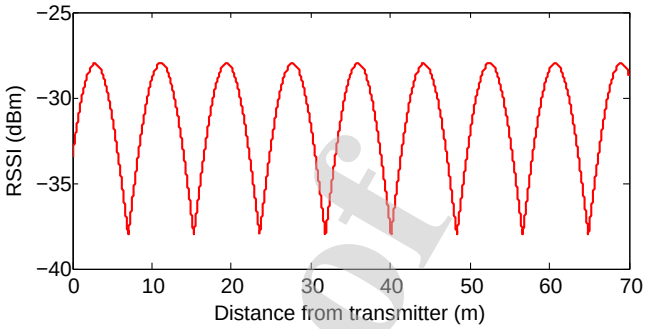

Fig. 2. Simulation of bimodal propagation in a 4-m diameter pipe. The interaction between two modes causes periodic spatial fadings. The maxima and minima of the fadings will be used as triggers in a discrete localization approach, while the signal model will be used as an RF map in a continuous approach.

Another approach, using sound instead, is presented in [19]. The idea is to build a map of the vibration signals induced by a hydrophone in a metal pipe and use this map and a Kalman Filter (KF) or Particle Filter (PF) for location purposes. Nevertheless, this approach has not been taken beyond a small lab experiment.

In a previous work [20], we first presented the results of an extensive analysis of RF propagation in a metallic pipe under different transmitter-receiver setups, demonstrating that it is possible to obtain periodic fadings. It is important to highlight that we refer to large-scale fadings in a spatial domain, which is a standing wave pattern that can be obtained in pipes and tunnels under certain configurations (that we explain in Section II), in contrast to the well-known small-scale fadings, understood as temporal variations in a channel. As an example, Fig. 2 shows these RF spatial fadings as a function of distance after displacing a receiver 70 m from the transmitter inside a pipe.

In that paper we furthermore explored the use the periodic fadings to design, first, a discrete RF odometry-like method to localize a robot inside a pipe. The periodicity of the RF signal together with an adapted version of the well-known Monte Carlo Localization (MCL) system is exploited in [21] to extend the methodology presented in [20] from a discrete localization to a continuous solution, using the periodic fadings as an RF map. One of the main advantages of these approaches over other RF-based previously cited methods is that there is no need to previously adapt the infrastructure, the only requirements being the placement of a continuous wave transmitter at the starting point and a receiver on the robotic platform in order to generate and detect the periodic fading waveform respectively. Metallic pipes have a low attenuation rate, providing us with a maximum possible coverage length of several kilometers if the right RF frequency is chosen, as we will show later. Moreover, there is no need for a previously known map of the environment.

The approach proposed in this paper builds on the aforementioned work. The main contributions of the present study can be summarized as follows:

- First, a thorough analysis of the received RF power in pipes is carried out in the transverse (cross-section) dimension, extending the longitudinal studies performed in [20].
- The phase difference (spatial phase shift) obtained with multiple receivers resultant from this analysis is used to improve the resolution of the discrete localization system presented in [20], as well as the accuracy and reliability of the continuous localization approach described in [21].
- Localization experiments performed in [20] are extended from a laboratory-scale pipe to a real drainpipe (4-m diameter and over 300-m long) in a dam in Castillonroy, Spain.
- Lastly, an EKF and a particle filter for the continuous solution are compared and some key considerations are outlined for the use of the RF approach with different robot platforms.

The paper is structured as follows. In the next Section, a summary of RF propagation in pipes together with experimental results are presented, while Section III details the effect of the antenna position in the pipe cross-section over the fadings, in order to improve the localization. Section IV describes the experimental setup. Section V formulates the discrete robot localization method together with the results obtained in the real pipe, followed by the continuous localization method and its experimental validation using one (Section VI) and then two signals (Section VII). In Section VIII, the practical considerations for real implementation are discussed and summarized. Finally, the conclusions are set out in Section IX.

II. Summary of RF Propagation in Cylindrical Waveguides and the Appearance of Periodic RF Fadings

As this work presents a localization method based on periodic fadings (by means of traversing them or using them as a map), given a pipe it is of special interest to determine the frequency of operation to obtain these fadings, their period, and their amplitude. This section presents a generic form of the expressions for practical purposes, while the formal derivation of the expressions is addressed in Appendix A.

In free space an antenna produces spherical waves that have a non-isotropic spatial distribution, corresponding to the radiation pattern of the antenna. The radiated power is spread over a surface that grows as r^2, and thus the power density decays as $1/r^2$ in the best case.

If the antenna is placed inside an air filled pipe or tunnel-like cavity, the spherical wavefronts will be multiply scattered by the surrounding walls. The energy is condensed in this area, improving the free space decay, and the resultant wave propagates with a standing wave pattern which, depending on the frequency, shows spatial fadings such as those seen in Fig. 2.

The interaction between these 'bouncing waves' can be studied using ray tracing theory or modal theory. The ray tracing theory models these waves as different rays, which travel in different paths causing constructive and destructive interference, and hence, fadings.

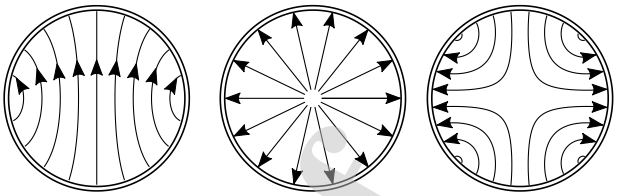

(a) TE_{11} - mode 1 (b) TM_{01} - mode 2 (c) TE_{21} - mode 3

Fig. 3. Field structure (lines) for the first three propagating modes inside a metallic cylindrical waveguide

In this work we have adopted the modal theory approach, as the geometric interpretation of the modes (analog to rays in the ray tracing theory) allowed for the explanation of the transversal structure of the fadings.

Related to the propagation modes, it is important to highlight that:

- The modes classified in TE (Transversal Electric modes, with no electric field component in longitudinal direction) or TM (Transversal Magnetic modes, with no magnetic field component in longitudinal direction), and are further indexed with two integer subscripts (p=0,1,2,3... , q= 1,2,3...), that account for the mode structure across the pipe. The first three propagating modes, relevant for this work, are TE_{11}, TM_{01} and TE_{21}, which we will also call mode 1, mode 2 and mode 3 respectively.
- Each mode describes a geometrical arrangement of the electromagnetic fields in the guide cross-section (see Fig. 3).
- For each mode there is a cutoff frequency (which depends on the pipe diameter), and the mode propagates if the operating frequency is above it.
- Each mode has its own wavelength in the waveguide (different from the free space one).
- The transmitting and receiving antennas position and orientation are relevant for the modal coupling. For practical purposes, aligning the antenna with the electric field lines enhances the power coupling, while placing it perpendicular diminishes it.

For each mode there is a cutoff frequency (for simplicity, f_{cn} for the n_{th} mode). For an air filled cylindrical pipe of radius a:

$$f_{c\,n} = \chi_{pq}\frac{c}{2\pi a} \tag{1}$$

for TM modes, and:

$$f_{c\,n} = \chi^{'}_{pq}\frac{c}{2\pi a} \tag{2}$$

for TE modes. c is the free space speed of light, χ_{pq} is the q_{th} zero of the Bessel function J_p of the first kind and $\chi^{'}_{pq}$ is the q_{th} zero of $J^{'}_{p}$, the derivative of the Bessel function J_p of the first kind. The mode with the lowest cutoff frequency is called the dominant mode and is the TE_{11} with $\chi^{'}_{11}$ = 1.8412. The next two cutoff frequencies correspond to TM_{01} with χ_{01}=2.4049 and TE_{21} with $\chi^{'}_{21}$ = 3.0542. These values are constants.

If $f > f_{cn}$, the mode's wavelength is given by:

$$\lambda_n = \frac{\lambda}{\sqrt{1-\left(\frac{f_{cn}}{f}\right)^2}} = \frac{c}{f\sqrt{1-\left(\frac{f_{cn}}{f}\right)^2}} = \frac{2\pi}{\beta_n} \quad (3)$$

where β_n is the phase constant and will be used in Eq. (5) to calculate the fadings amplitude.

If only the first two modes - which have different wavelength - are present (i.e. $f_{c1} < f_{c2} < f < f_{c3}$), the phase delay accumulated by each one will be different for a given travel distance d. The superposition of the electric field of the modes will take place with different relative phases in different positions inside the guide, producing constructive interference where both modes are in phase and destructive interference where the relative phase differs by an odd multiple of π. This gives rise to periodic fading in the RF power available inside the waveguide. The spatial period of this fading structure D is the distance that creates a relative phase of 2π between the two modes considered:

$$D = \frac{\lambda_1 \lambda_2}{|\lambda_1 - \lambda_2|} \quad (4)$$

When more than two propagating modes are present, every possible pair of modes will create a fading structure with its own characteristic spatial period, giving rise to an intricate available power distribution inside the guide. Even in this case, knowing the shape of the modal fields, careful selection of the transmitter and receiver antenna position and orientation in the pipe cross-section can lead to a system that, in fact, operates as if only two modes were present, minimizing the coupling to the unwanted modes on the transmission and/or reception side.

In [20] we show the results of a serie of field tests to characterize these fadings. The propagation experiments were performed in a 300-m long and 4-m diameter pipe by placing a transmitter at the beginning of the pipe and displacing a receiver along the pipe at constant speed while recording the RSSI. Here we summarize the relevant cases given the number of propagating modes. For reference, Table I shows the cutoff frequencies for the first four modes for this pipe, derived from Eqs. (1) and (2).

- $f < f_{c1}$. *Below cutoff frequency:* the expected behavior of the signal is a rapid attenuation, as the pipe does not act as a waveguide for these frequencies. See Fig. 4 for experimental results below the first mode's cutoff frequency ($f = 40$ MHz, while $f_{c1} = 43.95$ MHz).
- $f_{c1} < f < f_{c2}$. *Monomodal propagation:* usually used to transmit signals for communication along a waveguide, as it avoids interference with higher order modes. No fadings are obtained in this setup, as seen in Fig. 4. However, if one of the extremes of the pipe is closed (not the case in this work), the propagating wave will reflect off the closed end and travel in the opposite direction of the incident wave, producing interference and hence a standing or stationary wave pattern. The period of the fadings is one half of the wavelength of the signal in the pipe (Eq. 3). See Chapter 5.2.3.2 of [22] for more details.
- $f_{c2} < f < f_{c3}$. *Bimodal propagation:* interference between the first two modes (TE_{11} and TM_{01}), producing periodic fadings.
- $f_{c3} < f < f_{c4}$. *Trimodal propagation:* interference between the first three modes. The reason to explore this propagation is because the interference between the first and third modes causes shorter period fadings than that between the first and second or that between the second and third modes. As the goal is to localize a robot using the fadings (e.g. counting the fadings while traversing them in a discrete approach), the shorter the period, the higher the resolution. Unfortunately, selecting a frequency to excite the first and third modes also involves exciting the second one. The solution for eliminating the influence of the latter was based on taking advantage of the geometry of the modes to choose an emitter-receiver configuration with enhanced sensitivity for the first and third modes, while diminishing the second mode. From Fig. 3, it can be seen that the second mode has radial symmetry. This means that, for instance, centering the transmitting antenna perpendicular to the vertical axis and close to the floor will couple the least power to the second mode (i.e. the antenna and the electric-field lines are perpendicular), while aligning to the field lines of the first and third mode.
- $f_{c4} < f$. *Multimodal propagation*. Complex RF fading structure not relevant for this work. See [20].

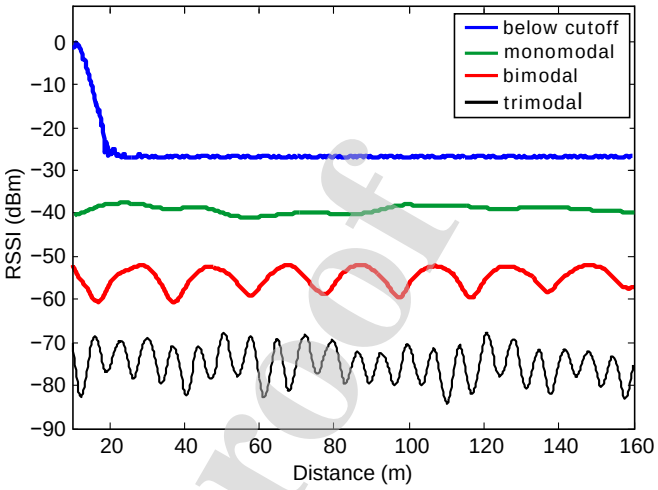

Fig. 4. Different propagation scenarios in Castillonroy, from [20]. Below the cutoff frequency ($f = 40$ MHz) the signal completely attenuates within about one wavelength. Therefore, this setup is not useful either for communication or for localization purposes. On the other hand, the monomodal propagation ($f = 51$ MHz) shows a signal with little attenuation along the pipe. Although useful for communication purposes, this setup does not work for localization either. Bimodal ($f = 71$ MHz) and trimodal ($f = 75$ MHz) propagation produces RF fadings, being the period of the fadings shorter in the latter, in the same pipe.

Finally, for two modes, the power wave amplitude is defined as:

$$P(x) = K_1 e^{-\gamma_1 x} + K_2 e^{-\gamma_2 x} \quad (5)$$

TABLE I
CUTOFF FREQUENCIES FOR THE FIRST PROPAGATING MODES IN CASTILLONROY

	mode 1	mode 2	mode 3	mode 4
f_c (MHz)	43.95	57.41	72.91	91.47

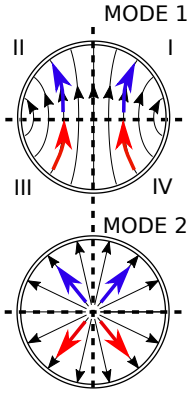

Fig. 5. Cases of interest to study constructive (blue arrows) and destructive (red arrows) interference between modes 1 and 2.

where $\gamma_n = \alpha_n + j\beta_n$ is called the propagation constant. Its real part, α_n , is the attenuation constant (Np/m) - usually negligible for the distances covered in our testbed, as metallic pipes have very low attenuation. Its imaginary part, β_n, is the phase constant (rad/m) and can be derived from Eq. 3. K_n is the complex-valued power wave rms amplitude of the n_{th} mode. The power wave amplitudes determine the signal model fading maxima and minima. The values of K_n can be estimated following the procedure outlined in Appendix A, or alternatively fitted to (or further refined with) experimental data. This last step will also take care of unavoidable deviations from ideality associated with, for example, obstacles inside the pipe (e.g. rocks or other robots), and junctions between different pipe sections.

For practical purposes, we will adopt the Received Signal Strength Indicator (RSSI) in the receiving antenna as the RF signal model $h(x)$, calculated as:

$$h(x) = 20\log_{10}|P(x)| \tag{6}$$

Summarizing, the pipe diameter determines the different

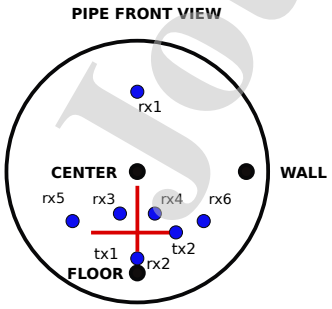

Fig. 6. Pipe front view. Transmitter-receiver positions for different cross-section fadings analysis.

modes' cutoff frequencies (as χ_{pq} and χ'_{pq} are constants). Selecting an operating frequency above certain mode's cutoff frequency allows to propagate that mode, together with the lower order modes. If there are two modes propagating and interacting, periodic fadings are obtained. The period of the fadings is a function of the operating frequency, and the pipe diameter (as it determines the cutoff frequencies). We encourage the reader to see [20] for results on more than three modes propagating, influence on the antenna polarization, stationarity of the signal and repeatability of the fadings. At last, we extend this analysis for non-ideal pipes (with experimental results) in Appendix B, addressing the effects of the pipe length, presence of obstacles, curved sections and so on; showing that the localization algorithms detailed in Sections V - VII would be viable not only in ideal waveguides but also in a wide range of real world pipes with slight to moderate defects and cracks, suffering from local deformations and/or obstacles present.

III. TRANSVERSAL FADINGS

Having studied the fadings along the longitudinal dimension, in particular, the cases of bimodal and trimodal propagation, we move on to analyze the transversal structure of the fadings. That is, we have studied the effects of the cross-section position on the received power and relative phase of the fadings (i.e. are the fadings the same if I navigate with the antenna in the left or right side of the pipe?). By analyzing the electric field distribution of the first three modes (Fig. 3), together with the practical placement of two receivers in a robot, two cases emerge as relevant for analysis: virtually dividing the pipe with respect to the center horizontally (upper vs lower half) and vertically (right vs left half).

Along this section, the approach is to analyze the agreement or disagreement between the zones of interest (left vs right, up vs down) regarding to if the electric-field lines of the two modes interacting add positively (both lines go in the same direction, represented with blue arrows in Fig. 5), or the contrary case (represented with red arrows). We will see that an agreement translates into the same spatial phase (both signals with matching maxima and minima), while a disagreement translates into a phase delay of 180 degrees (a maximum in one signal matching a minimum in the other).

As an example, consider the case of bimodal propagation (modes 1 and 2, Fig. 5). After virtually dividing the pipe horizontally and vertically (quadrants I to IV), lets place one receiver vertically oriented in quadrant I. In this position, the electric-field lines of modes 1 and 2 add positively (same electric-field lines directions for both modes in the same quadrant, represented with blue arrows). If a second receiver is placed vertically oriented in quadrant II, the case is the same, and hence, the received signal of both receivers will match quite well (same phase).

Consider that we move both receivers to the lower half (quadrants III and IV). The electric-field lines now add negatively. Despite appearing an opposite case to the previous, in the context of the relative phase between two signals, as both cases match (both add positively or both add negatively), the relative phase will be the same in both of them.

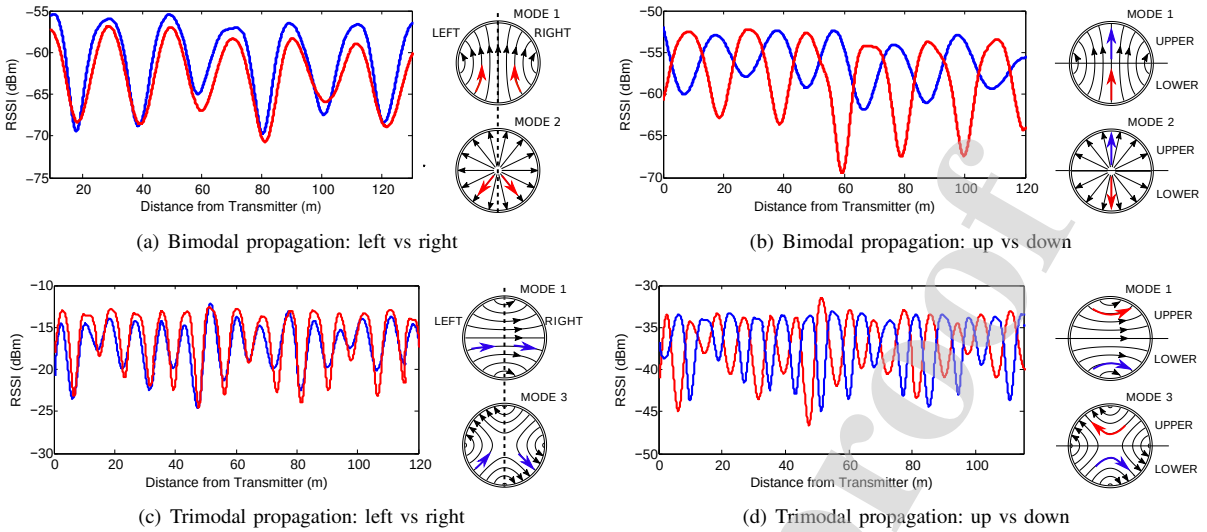

(a) Bimodal propagation: left vs right

(b) Bimodal propagation: up vs down

(c) Trimodal propagation: left vs right

(d) Trimodal propagation: up vs down

Fig. 7. Received signal power in the left and right half ((a) and (c)) vs upper and lower half((b) and (d)), together with the electric field distribution for: bimodal propagation ((a) and (b)) and trimodal propagation ((c) and (d)). The blue arrows represent constructive interference between the electric fields of the two modes interacting, while the red arrows the opposite.

TABLE II
TRANSVERSAL FADING ANALYSIS CASES

CASE	TRANSMITTER	RECEIVERS	MODES COUPLING	RELATIVE PHASE
1 - Bimodal left-right (Fig. 7(a))	tx1 vertical	LEFT rx3 vertical	OPPOSITE	0°
		RIGTH rx4 vertical	OPPOSITE	
2 - Bimodal upper-lower (Fig. 7(b))	tx1 vertical	UPPER rx1 vertical	CONSTRUCTIVE	180°
		LOWER rx2 vertical	OPPOSITE	
3 - Trimodal left-right (Fig. 7(c))	tx2 horizontal	LEFT rx5 horizontal	CONSTRUCTIVE	0°
		RIGTH rx6 horizontal	CONSTRUCTIVE	
4 - Trimodal upper-lower (Fig. 7(d))	tx2 horizontal	UPPER rx1 horizontal	OPPOSITE	180°
		LOWER rx2 horizontal	CONSTRUCTIVE	

Now consider placing one receiver vertically oriented in quadrant I and another one in quadrant IV. Now, the interacting modes 1 and 2 add positively in the upper half while negatively in the lower half, which would translate into a signal phase delay of 180 degrees.

Table II together with Fig.7 show the setup and results of the experiments to corroborate this, for the case of bimodal and trimodal propagation, using two receivers in appropriate positions (refer to Fig. 6). The selected frequencies and antenna setups were chosen to produce bimodal and trimodal propagation. Also, recall that the transmitter position and orientation allows to enhance/diminish the power coupled to the modes of interest. In a similar manner, the receiver antennas were oriented to align with the field lines of the modes of interest.

By analyzing the results we can see that:

- As expected, the fading period in the case of trimodal propagation (cases 3 and 4 in Table II, Figs. 7(c) and 7(d)) is shorter compared to the case of bimodal propagation (cases 1 and 2, Figs. 7(a) and 7(b)).
- The fadings are in phase in the left vs right halves (cases 1 and 3, Figs. 7(a) and 7(c)), while there is a phase delay of 180 degrees in upper vs lower half (cases 2 and 4, Figs. 7(b) and 7(d)). This matches our analysis considering the explored receivers' positions.
- Also, notice that the electric-field lines of the first mode are 90 degrees rotated comparing cases 3 and 4 (Figs. 7(c) and 7(d)) with cases 1 and 2 (Figs. 7(a) and 7(b)), as explained in the previous section.

The phase difference will be exploited in the next sections to improve the robustness and resolution of the fadings-based localization algorithms.

A. Cylindrical symmetry considerations

Due to the azimuthal symmetry of the pipe, if the transmitter setup is rotated, the interpretation set out above is rotated as well. For instance, if the transmitter is placed horizontally at the floor operating at a frequency that results in trimodal propagation, there is a phase difference of 180 degrees between the lower and upper half, and the same phase between the left and right half. However, if due to practical reasons when installing the receivers on the robot we desire the phase delay between the left and right half (instead of upper and lower half), notice that a 90 degree rotation of the pipe setup (i.e. transmitter placed vertically close to the wall) will achieve so. Fig. 8 illustrates the situation.

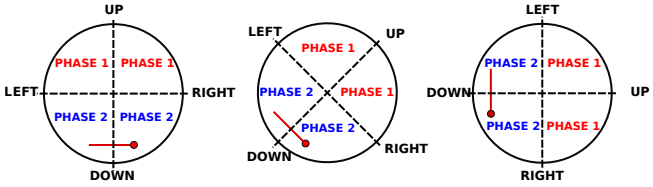

Fig. 8. Effects of rotating the antenna setup on the cross-sectional structure of the fadings. The phase difference between *phase 1* and *phase 2* is 180 degrees.

(a) Straight and tilted parts of the pipe

(b) Instrumented Pioneer P3AT robot inside the pipe carrying two horizontal antennas.

Fig. 9. Large-scale pipe experimental setup

IV. Test Scenario and Experimental Setup

For localization purposes, the test scenario was a 300-m long carbon steel pipe with a 4-m internal diameter used as a drainpipe for the Santa Ana dam in Castillonroy, Spain. It consists of two inclined parts (at the beginning and the end, tilted 23 and 30 degrees respectively), and a 120-m straight section (Fig. 9(a)).

To analyze the propagation behavior, a B&K Precision 2005B RF Signal Generator was used as the transmitter (tx). The transmitter antenna was longitudinally fixed at 10 m from the beginning of the straight section of the pipe, and its cross-section position and orientation will be specified for each experiment.

A Pioneer P3AT differential drive robot was used as the moving receiver/service robot. The platform was equipped with two RF Explorer model 3G portable spectrum analyzers as RF receivers (in order to exploit the spatial diversity), two odometers, an Xsens MTI 100 IMU, and a SICK LMS200 laser range sensor (Fig. 9(b)). As the pipe has no structural features, a series of landmarks were added at the laser field-of-view level for ground truth purposes. All the sensors were connected to a computer running Robot Operating System (ROS) on Ubuntu.

V. Discrete Robot Localization using RF Signal Fadings

The previously presented study, supported by experimental validations, allowed to propose an RF-based localization method alternative to those existing in the literature. We have studied the setups (more specifically the operating frequency and tx-rx positions) to obtain periodic spatial fadings inside a metallic pipe, where the period is determined by the RF transmitter's operating frequency and the radius of the pipe. As a first approach we have developed a discrete localization method, where the idea is to count the (known-period) fadings while traversing them. Furthermore, we have then improved this method in a continuous approach using the fadings model. In both cases, we have first used only one signal (from one receiver), and subsequently we have exploited the spatial diversity which allowed to improve the resolution and robustness in both approaches, by means of using two received signals. In the following sections we derive the formulations together with the experimental results obtained in a real scenario.

A. Algorithm formulation

While displacing the RF receiver from the transmitter, the basic strategy of the algorithm is to discretely determine the distance traveled (one-dimensional localization in the longitudinal axis), by counting the fadings maxima and minima encountered (e.g., detecting the changes in the slope), creating a type of RF-odometry. As two changes in the slope take place within one fading (minimum and maximum), the localization resolution is equal to half of the (easily calculated) period of the fading. In this case, the shorter the period, the better the localization resolution. Finally, the direction of motion is used to increase or decrease the distance traveled after detecting the changes in the slope. Fig. 10 illustrates the algorithm by means of simulating bimodal propagation in a generic metallic pipe (although it can be extrapolated to any periodic signal).

Moreover, if two receivers are used, the algorithm can be improved in terms of robustness and resolution. If the signals are in phase (e.g., Fig. 7(c)), redundancy can be used to improve the robustness. If the signals are phase-delayed (Fig. 7(d)), two more triggers can be perceived within a fading, where the two signals cross each other. These two extra triggers allow us to improve the localization resolution from a half to approximately a quarter of the period of the fading (see Fig. 11).

B. Experimental results

In order to check the validity of the proposed algorithm in a real situation, the Pioneer P3AT wheeled robot was placed

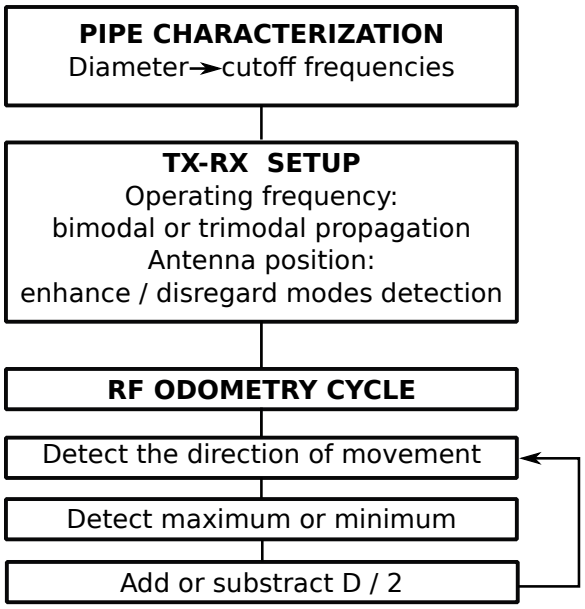

(a) Diagram

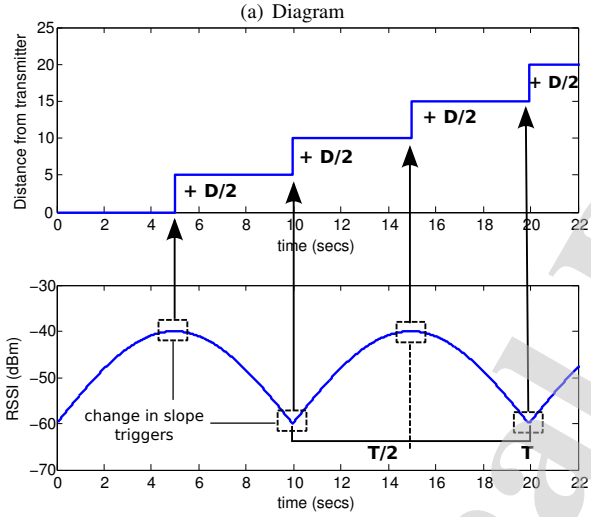

(b) RF odometry

Fig. 10. Discrete Localization: (a) Algorithm and (b) Example using a generic periodic signal. T denotes the time period of the fadings, and the dashed squares the changes in the slope used as triggers, adding $D/2$ to the current position each time detected (D being the spatial period of a fading).

inside the Santa Ana dam drainpipe, simulating a service routine. The robot traveled in a straight line for about 70 m at a mean speed of 0.5 m/s, and hence, the heading variations are negligible.

To obtain shorter period fadings, trimodal propagation was chosen. The frequency selected was f=78.2 MHz, producing fadings with a period of 8.26 m and a discrete localization resolution of 4.13 m. The transmitter antenna was placed horizontally at 1 m from the floor (position $tx2$ in Fig. 6), and the two receivers at 1.5 m and 2.5 m in height (0.5 m above and below the center of the pipe). With this configuration, a relative phase difference of about 180 degrees is expected between the receivers. The above described experimental setup was used for both the discrete and the continuous localization.

Fig. 12(a) shows the results for the position estimation using

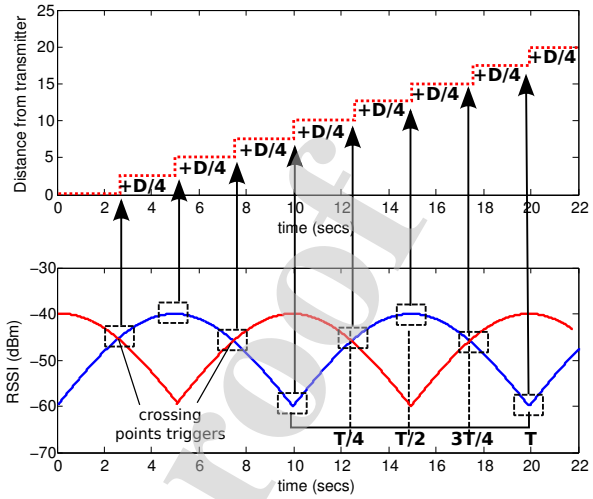

Fig. 11. Effects of exploiting spatial diversity. By means of adding the 'crossing point' triggers, the discrete resolution is improved to $D/4$ (D being the spatial period of a fading)

four methods. The black line shows results from the localization method used in [23], which combines information from the odometers and the laser sensor lain over the previously built and corrected map of the pipe, with the added structural landmarks. We consider this the ground truth. The green line shows a purely odometric position estimation, evidencing the cumulative errors and drift. The blue line shows the discrete position estimation from the fadings localization algorithm (with a resolution of half of the period of the fadings), using just one of the RF receivers. The fadings maxima and minima of the signal shown in Fig. 12(b) were used as triggers. Lastly, Fig. 12(c) shows the measured received power at each of the two receivers. It corroborates the expected relative phase difference of 180 degrees (a maximum in one signal that matches a minimum in the other), allowing the use of two extra triggers and improving the localization resolution. Results are shown in red in Fig. 12(a).

C. Practical Considerations

In an ideal case, where we have identical receivers and antennas, and under symmetry conditions, the phase delayed RF signal levels must be identical (but, of course, shifted). In this situation, the two signals cross each other at the same distance from the fading maximum or minimum, but the real implementation effects, including different behaviors in the antennas and distortions caused by the presence of the robots, produce differences in the two signals (one showing deeper fading than the other or being more attenuated). This means that, unlike in the ideal case, the signals do not cross each other at exactly the same point, and hence, the discrete resolution is not exactly one quarter of the signal of the fading. For this reason, the distance may be underestimated before a maximum and overestimated after it (or viceversa). This analysis is only valid, however, for the triggers where the signals cross each other, not applying at the maxima and minima, where this overestimation or underestimation error is reset. The situation is illustrated in Fig. 13. To solve this the model can be

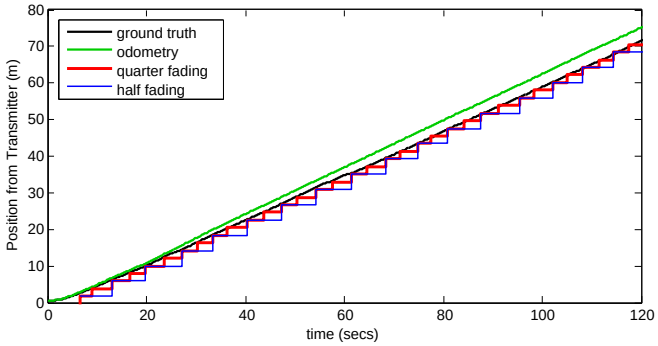

(a) Position estimation

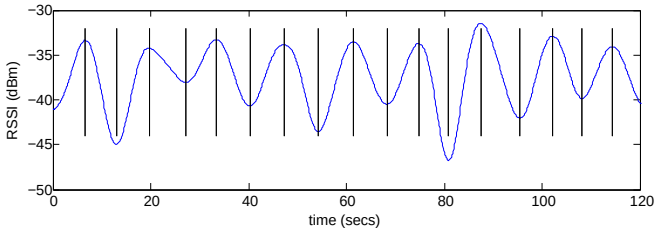

(b) Signal fadings using one receiver. The vertical lines denote the triggers

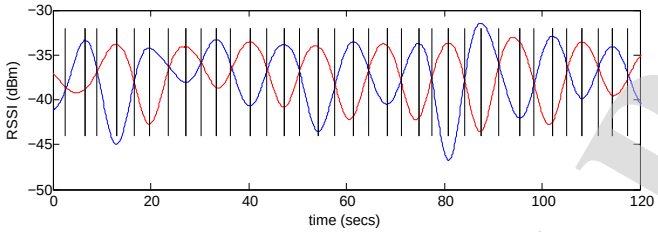

(c) Signal fadings using one receiver in the upper half and one receiver in the lower half of the pipe.

Fig. 12. Comparison of localization methods in the large-scale pipe

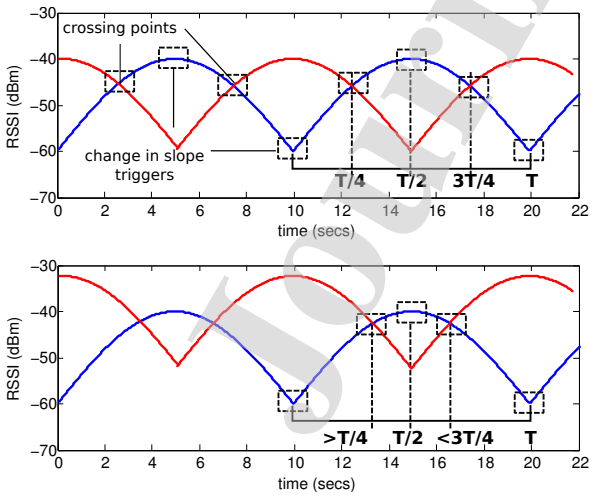

Fig. 13. Effects of having a power offset in the signals received. The 'crossing points' triggers displace, while the 'change in slope' triggers remain the same.

calibrated online, once one fading is traversed and hence the maximum and minimum are determined.

Furthermore, although not the case with these experiments, it is true that miscounting the number of maxima and minima that have been traversed (cycle slipping) would cause a more significant error in the position estimate. To address these issues, a more complex continuous approach which includes the signal model has been developed, as described in the following section.

VI. Continuous Robot Localization using one RF Signal Fadings

The next natural step was to extend the methodology presented in the previous section from a discrete localization to a continuous solution, taking advantage of the periodic nature of the RF signal.

As has been shown in Section II, the fadings waveform and its period can be calculated without the need for previous experimental measurements inside the pipe (see Eqs.(4)-(5)). Each longitudinal position of the pipe has an associated RSSI value, meaning that this model serves as a unidimensional map (herein the RF Map).

The goal is to obtain continuous robot localization along the pipe. For this purpose, let the state of the robot x_t at time t be calculated using its motion model f:

$$x_t = f(u_t, x_{t-1}) + \epsilon_t, \epsilon_t \sim \mathcal{N}(0, V) \tag{7}$$

where u_t are the control inputs at time t and ϵ_t is a random variable that models the uncertainty introduced by the state transition based on variance V. Due to the cylindrical shape of the pipe, the robot travels in a straight line and only slight heading variations are observed. Therefore and from now on, the state x_t will refer to position x along the pipe.

During the displacement of the robot, the observations z_t at time t are provided by the sensors. The non-linear measurement model h relates the observations to the state of the robot x_t:

$$z_t = h(x_t) + \delta_t, \delta_t \sim \mathcal{N}(0, W) \tag{8}$$

where δ_t corresponds to the uncertainty of the measurement represented by a random noise based on variance W.

In our RF approach, the RF signal model (Eq. (6)) is used as the measurement model:

$$h(x_t) = 20 \log_{10} |(K_1 e^{-\gamma_1 x_t} + K_2 e^{-\gamma_2 x_t})| \tag{9}$$

where we have converted to RSSI in dBm units with K_p in $mW^{-1/2}$ units.

Following this general formulation, the strategy proposed in [21] relies on an adapted version of the Monte Carlo Localization (MCL) system [24] using the RF signal model as an RF Map.

As is well known, MCL is a probabilistic method based on particle filters where the posterior distribution of the state is represented by a set of weighted particles x_t^m. It solves the localization problem through the following typical steps: particle filter initialization, prediction, weighting of the

particles and resampling. Once the filter is initialized with a set of particles, during the prediction step, the state of each particle x_t^m is updated based on its sample motion model:

$$x_t^m = f(u_t, x_{t-1}^m) + \epsilon_t \tag{10}$$

where u_t corresponds to the inputs of the system, linear and angular speed (v_t, w_t).

The main contribution of [21] takes place during the weighting step. Similarly to the typical matching process between laser scan measurements and a previously known grid map, the measurements provided by the RF sensor are compared with the RF Map.

The Gaussian probabilistic density function was chosen to calculate the weight that represents the probability of each particle to be a good hypothesis of the actual position:

$$w_t^m = e^{-\frac{1}{2}\left(\frac{z_t - \hat{z}_t^m}{\sigma}\right)^2} \tag{11}$$

where σ^2 (L) is the variance of the likelihood function applied to the innovation process, z_t is the actual observation and $\hat{z}_t^m$ is the expected observation for the m-th particle calculated using the RF signal model as the measurement model similarly to Eq. (9):

$$\hat{z}_t^m = h(x_t^m) \tag{12}$$

Based on the results presented herein, we can conclude that the proposed continuous localization method provides good performance and improves on the position resolution presented in [20]. Moreover, it overcomes the lack of distinctive features in pipes.

The starting point for the main contributions of the present work in terms of continuous localization inside pipes comes from this analysis.

A. Variable RF sensor measurement model variance

During the validation of the previously described method, the uncertainties involved in the algorithm were modeled using constant variance values provided by data sheets. After studying the experimental results, it is clearly seen how the uncertainty of the system increases in areas close to the highest values of the RF signal where the signal is flattened. The greater the number of possible positions corresponding to similar RF values, the wider the particle distribution and the greater uncertainty. On the contrary, the uncertainty decreases in areas close to the valleys of the signal (fadings), where the particle distribution becomes significantly narrower. Fig. 14 illustrates the aforementioned characteristics of the RF signal model and the actual RF measurements. To take into account this behavior, we propose an improvement involving use of a variable function for the variance related to the measurement model of the RF signal (W) instead of a constant value.

The goal is to obtain a transfer function which provides variance values with the same shape as the RF signal model. In this way, the applied variance will increase or decrease replicating the observed behavior. The variance value at each

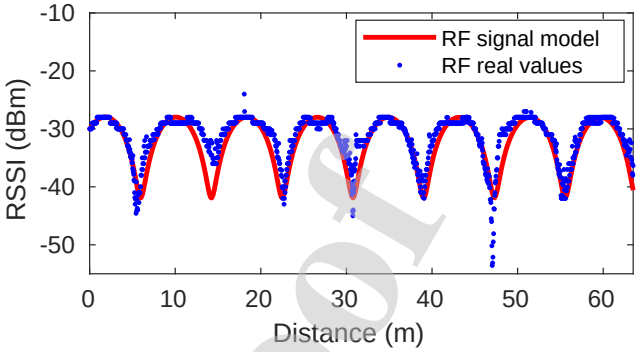

Fig. 14. RF signal model vs RF sensor measurements (dotted). The signal is more flattened close to the maxima, resulting in larger uncertainties. By contrast, the sharp form of the signal in the valleys results in smaller uncertainties.

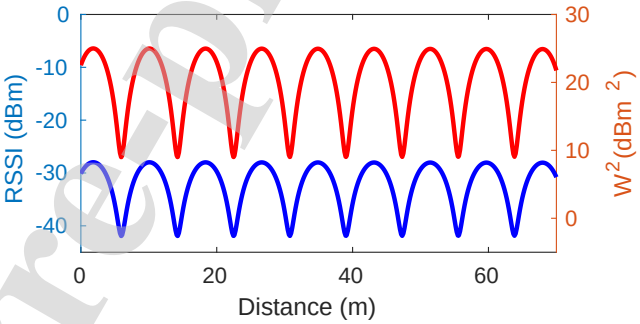

Fig. 15. RF signal model (blue) and sensor measurement model variance (red) for $W_{up} = 5^2$, $W_{low} = 3^2$ and $W_{offset} = 3^2$.

timestamp W_t^m for particle m will depend on the RSSI value of the RF signal model as shown in Eq. (13).

$$\begin{aligned} W_t^m &= (RSSI_{fm}^m - min(RSSI_{fm})) * f_{scale} \\ &\quad + W_{offset} \\ f_{scale} &= \delta_W / \delta_{RSSI_{fm}} \\ \delta_W &= W_{up} - W_{low} \\ \delta_{RSSI_{fm}} &= max(RSSI_{fm}) - min(RSSI_{fm}) \end{aligned} \tag{13}$$

where $RSSI_{fm}^m$ is the RSSI value corresponding to the position of particle m provided by the RF signal model (Eq.(9)) and f_{scale} is a scale factor to convert the RSSI value to a variance value (dB^2) between an upper and lower limit (W_{up}, W_{low}) taking into account the fadings model waveform amplitude $(\delta_{RSSI_{fm}})$. Finally, W_{offset} is the offset for the variance function. Fig. 15 provides an example of the resultant variance function together with the RF signal model.

As can be noticed from Fig. 14, the RF signal model along the pipe is similar enough to the RF sensor measurements in the real scenario to consider the bias error negligible.

B. IMU for prediction purposes

During the experimental validation of the work presented in [21], a differential robot was equipped with various different sensors. The linear and angular speed of the robot were provided by two encoders placed on the robot wheels. These

values correspond to the inputs of the system used during the prediction step of the algorithm.

There are other robotic platforms with which it is not possible to use mechanical odometry sensors (e.g., aerial robots). In order to check the feasibility of the proposed method in these types of platforms, we propose the use of the values provided by an IMU. The information given by this sensor is the linear acceleration and the angular speed that are applied to the motion model of the vehicle during the prediction step.

The results of the position estimation of the robot along the pipe using the IMU sensor during the prediction step are shown in the experimental results subsection.

C. Continuous localization system based on EKF and RF signal

The EKF [24] is one of the most popular algorithms for state estimation in robotics applied to non-linear systems. The posterior distribution at time t is represented by the system state X_t and the covariance P_t. The EKF overcomes the Kalman Filter assumption of linear state transitions and linear measurements by means of a linearization process. Its strength lies in its simplicity and in its computational efficiency. In order to evaluate its feasibility for the localization of the robot inside pipes, an EKF algorithm was implemented using the RF signal.

During the EKF prediction step, the state of the robot $\hat{X}_t$ is propagated according to the motion model (Eq. (7)):

$$\begin{aligned} \hat{X}_t &= f(u_t, X_{t-1}) \\ \hat{P}_t &= F_t P_{t-1} F_t^T + G_t V G_t^T \\ F_t &= \partial f / \partial_X \\ G_t &= \partial f / \partial u \end{aligned} \tag{14}$$

where $\hat{P}_t$ is the predicted covariance, f refers to the motion model of the vehicle, u_t are the inputs of the system (v_t, w_t) and (F_t, G_t) are the Jacobians calculated as the partial derivatives of the function f with respect to the state variable x and with respect to the inputs of the system u respectively. V is the variance associated with the vehicle odometry uncertainty.

The update step provides correction of the predictions by incorporating the measurements z_t:

$$\begin{aligned} X_t &= \hat{X}_t + K_t(z_t - h(\hat{X}_t)) \\ K_t &= \hat{P}_t H_t^T (H_t \hat{P}_t H_t^T + W_t)^{-1} \\ P_t &= (I - K_t H_t)\hat{P}_t \\ H_t &= \partial h / \partial_X \end{aligned} \tag{15}$$

In this particular case, the observation z_t is the RSSI value provided by the RF receiver sensor and the measurement model h corresponds to the RF signal model used to predict the expected observation $\hat{z}_t$ (similarly to Eq. (12)). W_t is related to the measurement model variance of the RF sensor.

The Jacobian H_t needed to calculate the Kalman gain of the filter is obtained through the derivative of the RF signal model equation with respect to the state variables.

The results provided by the application of the EKF to solve the localization problem inside pipes are presented in the following subsection together with a comparison between the two methods: particle filter versus EKF.

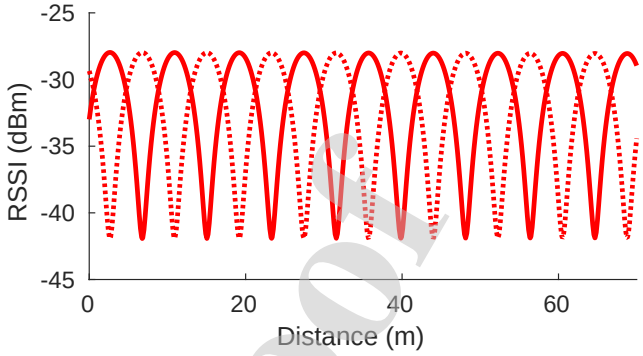

Fig. 16. Theoretical received signal corresponding to the upper half and lower half of the pipe for trimodal propagation.

D. Experimental results

In order to check the validity of the continuous localization methods in a real situation, all the algorithms described in previous sections were implemented in MATLAB and tested with real data collected during the experiments described in Section IV at the Santa Ana dam in Castillonroy, Spain (Fig. 9(a)).

Given the operating frequency of 78.2 MHz, the inner pipe diameter of 4-m, and assuming an electrical conductivity of 4.5x10^6 S/m and a relative permeability of 100 (typical values for carbon steel), the propagation constants obtained using Eqs. (22) and (32) are $\gamma_1 = \alpha_1 + j\beta_1 = 0.0001 + j1.356m^{-1}$ and $\gamma_2 = 0.0005 + j0.595m^{-1}$. The power wave amplitudes K_1 and K_2 can be determined offline or even adjusted online in a practical approach, once the first fading is traversed, given that the sum of the power amplitude of both modes is equal to the fading maximum, while the subtraction of both equals the fading minimum. The online adjustment of the power wave amplitudes would solve the potential disparity between the theoretical model and the actual signal in case of systematic errors (bias) in the RF sensors. The values obtained were K_1 = 0.024 and K_2 = 0.016 $mW^{-1/2}$ (which actually adjust the total radiated power to -26 dBm, matching fairly good with our setup). Using all this data, it is possible to calculate the theoretical electromagnetic propagation along the pipe that will play the role of an RF Map (Fig. 16). Recall that the period of the fading is never adjusted, it is easily theoretically calculated (given only the radius of the pipe and the operating frequency), and that the electrical conductivity and relative permeability only influence on the attenuation, which is relatively small in metallic pipes.

The real data collected during the experiments were:

- Linear and angular speed (v, w): These values are provided by the odometry sensors and correspond to the linear and angular speed of the robotic platform, used in the prediction step of the continuous localization methods.
- Linear acceleration and angular speed (a, w): Data provided by the IMU corresponding to the linear acceleration

and angular speed. The state of the vehicle is predicted with these values when the IMU is used instead of the odometry sensors.
- RSSI values (z_1, z_2): These sensor measurements are provided by the RF receivers placed at different heights and are used in the update step of the different proposed methods.
- Ground truth: The real localization of the robot corresponding to the distance from the transmitter, obtained as explained in Section V-B. This value is used to compare the estimated pose of the robot provided by the localization algorithms with the robot real position. From now on, pose estimation error refers to the absolute value of the difference between the estimated position and the ground truth.

For the results described in this section, only one signal is used in the implemented algorithms (i.e., z_1 and its corresponding RF signal model from Eq. (6)).

In order to model the uncertainty of the elements involved in the system, some variance values must be defined:

- V: variance associated with the uncertainty of the vehicle odometry.
- L: variance of the likelihood function used during the particle filter weighting process.
- W: variance to model the uncertainty of the measurement model.

1) Results of the localization algorithm based on RF fadings and particle filters using the IMU during the prediction step: The continuous localization method presented in [21] fuses the information that comes from two different sources, one based on odometry and the other on the periodic RF signal inside pipes. A detailed description of the results obtained during the experimental validation can be found in Section IV of that work.

In the case of ground platforms, the odometry data is provided by encoders placed on the wheels. As stated before, in order to check the validity of the method with other robot types where the use of encoders is not feasible (e.g., flying robots), the IMU data collected during the experiments were used in the prediction step of the algorithm.

Several tests of the implemented localization method using the values provided by the IMU sensor were run to assess the stability and robustness of the solution. Fig. 17 shows the pose estimation error for different variance values:

- test 1: $L = 0.005$ and $V = 0.030^2$, mean error = 0.572 m
- test 2: $L = 0.001$ and $V = 0.100^2$, mean error = 0.552 m

The W variance is not selected as a constant value but obtained using the function of Eq. (13).

The cumulative error in the pose estimation when using only the odometry is clearly evident, whereas the position error remains limited around acceptable values when using the method based on particle filters. The results using the IMU as the main sensor for the prediction step are similar enough to the ones shown in [21] to suggest the feasibility

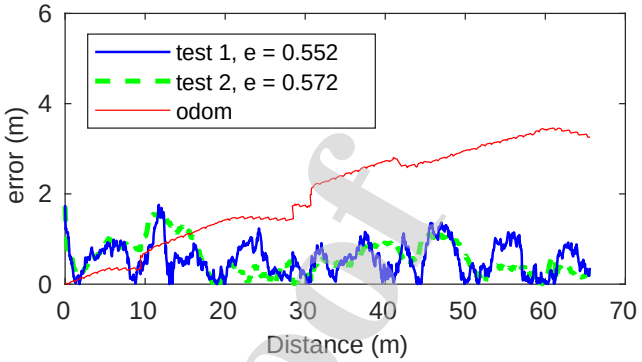

Fig. 17. Odometry and particle filter position estimation error during the displacement of the robot along the pipe using the IMU sensor in the prediction step. Red line: pose error using only odometry. Blue and green line, pose error using the particle filter solution for different values of variance (blue: $L = 0.005$ and $V = 0.030^2$, error = 0.572 m, green: $L = 0.001$ and $V = 0.100^2$, error = 0.552 m).

of the proposed localization method using different robotic platforms.

As it is well-known, although the use of the IMU sensor overcomes the errors derived from the slipping of the wheels in these types of environments, the pose estimated by integrating the IMU sensor readings easily drifts due to the sensor noise and time-varying biases. These effects could be even worse in the case of drones due mainly to vibrations. Usually in these systems, a combination of visual odometry with inertial systems is proposed to get a robust odometry [25]. Although it is beyond of scope of this work, our proposed method is expected to improve the odometry error of visual-inertial systems during the update phase by using the RF measurements, as the preliminary results of the experiments using the IMU during the prediction phase seem to indicate. Therefore, the proposed alternative method can be effective and should be evaluated when using different robotic platforms.

2) EKF results and comparison with particle filter method: An EKF implementation of the localization algorithm was developed following the same strategy of using the RF signal during the estimation process. The validation of the method was carried out using the data collected during the experimental tests. A small uncertainty value in the vehicle's odometry was needed for the EKF method to provide good results in the position estimation. For higher variance values related to odometry, the EKF method was unable to solve the localization problem during the displacement of the vehicle along the pipe.

In order to compare both particle filter and EKF solutions, the same variance values were selected for both methods:

- EKF: $V = 0.01^2$, $Wvar$, and $P_0 = 0.01^2$, where P_0 is the initial system variance.
- PF: $V = 0.01^2$, $Wvar$ and $L = 4$

Fig 18(a) shows the position error obtained with the EKF and particle filter methods compared to the odometry method. The estimated position calculated using the three different solutions is represented in Figs. 18(b) and 18(c). As can be deduced from the results, the EKF method does not perform as well as the particle filter method in terms of position estimation along the pipe. Nevertheless, the results are good enough to

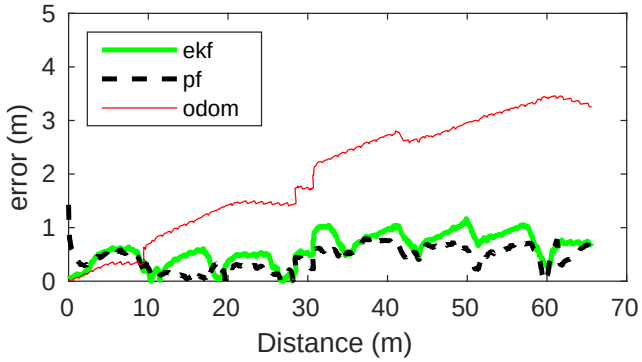

(a) Odometry, EKF and particle filter position estimation error

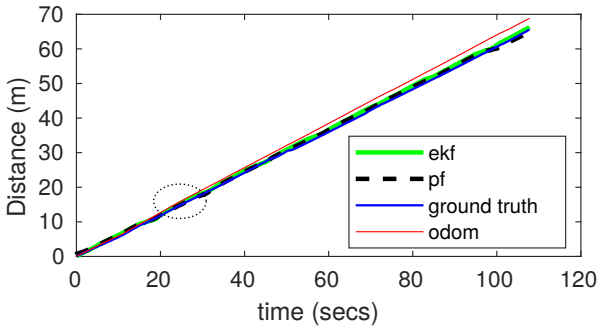

(b) Estimated position using odometry, EKF and particle filter

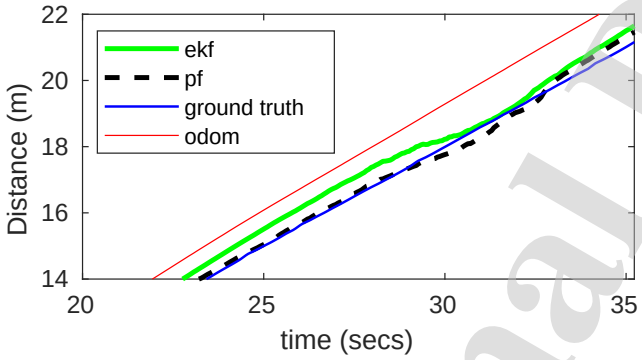

(c) Detail of estimated position within the dotted oval

Fig. 18. Comparison between EKF and particle filter during the displacement of the robot along the pipe: (a) Position error and (b)-(c) comparison of position estimation with EKF, particle filter and odometry methods with respect to the ground truth.

consider that the EKF method based on RF fadings may be suitable for localization inside pipes. For this reason, deeper analysis is required to evaluate the applicability of the EKF solution to solve this particular case.

A covariance analysis has been conducted in order to check the coherence of the application of the EKF algorithm to solve the localization problem using the RF signal. The evolution of the covariance during the displacement of the vehicle using both methods is shown in Fig. 19. As can be seen, the particle filter provides better results in terms of uncertainty than the EKF-based method.

In brief, although both methods provide good results in terms of vehicle localization inside the pipe, the use of the particle filter is more adequate due to the high non-linearity

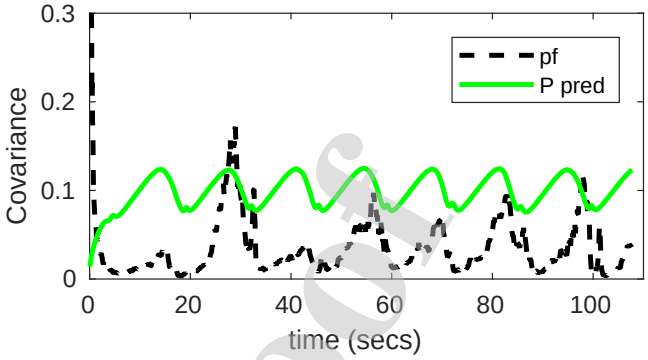

Fig. 19. Evolution of the covariance during the displacement of the vehicle using EKF and particle filter-based methods

of the RF sensor. Moreover, the position error is slightly better and the estimated position is closer to the real position of the robot when using the particle filter localization method. Apart from that, in order for the EKF method to provide a good solution, a small uncertainty of the state estimate is needed but in some cases, the assumption of a good odometry system is far from the real system. Therefore, we conclude that the EKF solution is less reliable compared to the particle filter.

VII. Continuous localization using two RF Signal Fadings

A. Algorithm formulation

As mentioned before in the transversal fadings analysis section, with a specific setup of the transmitter and receivers antennas in the pipe cross-section, a 180 degree relative phase difference appears between the fadings corresponding to each receiver. Fig. 16 represents the RF signal model of each transmitter-receiver configuration.

The phase difference between the two RF signals can be exploited in order to improve the accuracy and reliability of the localization algorithm presented in [21] that uses one single signal. Using the data provided by two RF receivers placed at different heights, twice as much information is available and it is possible to work with each signal with its own RF map.

We could formulate the problem as a regular robot localization issue where two sensors (e.g., LiDAR sensors) placed at different positions on the robot give information about the perceived environment. The positions provided by both scan-matching processes working with a known map are fused using the EKF algorithm. The approach presented consists of applying two independent particle filters, each of them working with an RF receiver, in a way that the resulting pose of each particle filter with its uncertainty is considered a virtual sensor. The information that comes from these virtual sensors is fused using the EKF algorithm in order to obtain the position of the robot along the pipe.

The goal of this method is to take advantage of the results of each particle filter in the areas where each of them works best, that is, where the particle distribution is the narrowest and therefore the uncertainty is the smallest. The less uncertainty in the pose estimation of the virtual sensor, the more influence this sensor will have in the EKF update step.

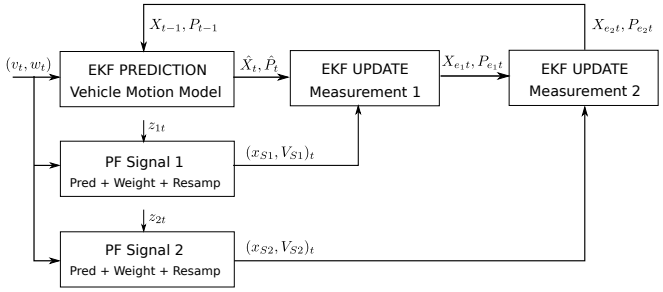

Fig. 20. Steps of the EKF localization algorithm with two RF signals. After the prediction step, the position and covariance $(\hat{X}_t, \hat{P}_t)$ are updated using the values resulting from the particle filter (x_{S1}, V_{S_1}) that works with the first RF signal. In a second correction step, the position and covariance obtained in the previous step (X_{e_1t}, P_{e_1t}) are updated using x_{S2} and V_{S_2} provided by the particle filter working with the delayed RF signal. The result of this step is the position and uncertainty of the vehicle at each time stamp (X_{e_2t}, P_{e_2t}).

In summary, the proposed method is based on the application of an EKF algorithm as the localization method using the pose estimations obtained through two particle filters working with both RF signals as measurements during the EKF update step (Fig. 20).

The main stages of the proposed method are:

1) EKF prediction: During this step, the state $\hat{X}_t$ and covariance $\hat{P}_t$ are predicted using the inputs of the system (v_t, w_t) and the odometry motion model (Eq. (14)).

2) Particle filter for each signal: As mentioned before, the steps of the particle filter are followed in order to obtain the estimated position. The RSSI value provided by the first radio frequency sensor (z_{1t}) along with its corresponding measurement model (Eq. (9)) are used in the weighting process to assign weights to each particle.

The result of the resampling step of each particle filter is a new particle distribution. The estimated position is obtained by calculating the mean position of the particles for each iteration. In the same way, the variance of the particle distribution is computed. Eq. (16) represents the pose estimate and its covariance for each iteration:

$$\begin{aligned} x_{S1} = \mu &= \frac{1}{M}\sum_{m=1}^{M} x_1^m \\ V_{S1} &= \frac{1}{M-1}\sum_{m=1}^{M} |x_1^m - \mu|^2 \end{aligned} \tag{16}$$

where M is the number of particles and x_1^m is the position of particle m.

Similarly, a second pose estimate is obtained using the RSSI value provided by the second receiver (z_{2t}) and its RF signal model. For symmetry reasons, the measurement model for this receiver placed at the upper half of the pipe (Fig. 7(d)) is represented by Eq. (17):

$$h(x_{2t}^m) = 20\log_{10}|(K_1 e^{-\gamma_1 x_{2t}^m} - K_2 e^{-\gamma_2 x_{2t}^m})| \tag{17}$$

To summarize, two pose estimates with covariances are available acting as virtual sensors to be used in the EKF update step: $(x_{S1}, V_{S_1}), (x_{S2}, V_{S_2})$

3) EKF update using the results of the particle filters as estimators: With the different virtual sensor measurements, which are characterized by an uncertainty level, a double correction step takes place using Eq. (15).

Firstly, using $(x_{S1}, V_{S_1})_t$ as the measurement and variance of the first virtual sensor respectively, the state and covariance predictions of the system ($\hat{X}_t$ and $\hat{P}_t$) are updated. Secondly, in a subsequent step, the results of the previous step X_{e_1t} and P_{e_1t} are again updated using the measurement and variance values corresponding to the second virtual sensor $((x_{S2}, V_{S_2})_t)$ obtaining X_{e_2t} and P_{e_2t}.

Therefore, the results of the EKF algorithm using a double correction step are:

$$\begin{aligned} X_t &= X_{e_2t} \\ P_t &= P_{e_2t} \end{aligned} \tag{18}$$

where X_t represents the estimated position of the robot along the pipe and P_t is the system covariance that represents the uncertainty of the calculated position.

It should be noted that, as the values provided by the virtual sensors are direct measures of the state, the Jacobian matrix H_t -that relates the state to the measurement needed for the Kalman gain calculation- is equal to the identity matrix.

B. Experimental results

Similarly to previous cases, the real data collected during the experiments described in Section IV was used to verify the improvement in the localization pose achieved by using two signals.

The number of particles for each particle filter is set to M = 1000. The particles are initially distributed along the first period of the fading of each RF signal in order to avoid the ambiguity problems derived from the periodic nature of the fadings waveform.

The variance values selected are the same for both particle filters:

$$V = 0.038^2; L_1 = L_2 = 0.007$$

The uncertainty in the measurement model W is obtained with Eq. (13) during the execution of the algorithm and the initial system covariance P_0 is set to 0.038^2.

Several tests were performed using the variance values selected in order to check the stability of the solution regardless of the probabilistic nature of the algorithm. Fig. 21 shows, for example, the position error obtained using the proposed localization method for three different tests with the same parameter configuration. As can be clearly seen, the mean error remains below 0.5 m, whereas the odometry error increases with time. These results demonstrate the adequacy of the variance values selected.

Moreover, the estimated position error using both signals improves on that obtained using one single signal as shown in Fig. 22(a). The uncertainty of the position calculated at each time-stamp for both virtual sensors is represented in Fig. 22(b). As expected, the virtual sensor with the least variance has the most influence on the EKF algorithm and

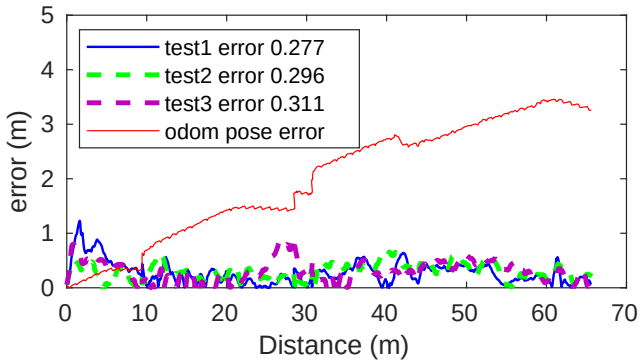

Fig. 21. Odometry and position estimation error as a function of the distance traveled (ground truth). Blue, green and purple curves represent the results of three iterations of the proposed algorithm using two RF signals. The same covariance values have been chosen for all the iterations.

the position predicted is corrected with the position estimated by the "best" virtual sensor. This behavior can be observed in Figs. 22(c) and 22(d) which show a detail of the area delimited by the dotted vertical lines. The uncertainty of virtual sensor 2 (green) is lower than the uncertainty of virtual sensor 1 (blue), and hence, the estimated position is corrected based on the position estimated by the former. Therefore, the error remains bounded around the smallest error at each timestamp. Fig. 23(a) shows a comparison of the estimated position over time using the different methods. The localization method based on the particle filter using only one RF signal (green and purple) closely follows the real position (blue). Similarly, the proposed algorithm based on the EKF using two RF signals (black) provides a reliable estimated position. But the latter, as can be seen in the detail shown in Fig. 23(b), corrects the position of the vehicle with the best solution of the two position estimators, in this case, the purple one. By contrast, the estimated position calculated using only the odometry (red) progressively moves away from the real position.

1) Coherence analysis: One of the assumptions of the EKF is the Gaussian distribution of the observations. As mentioned in the proposed method, the observations used in the update step correspond to the result of the particle filter with each radio signal. In order to evaluate the coherence of the application of the EKF algorithm, we analyzed the distribution of the particles resulting from both particle filters.

In order to accomplish this task, the set of particles obtained after the resampling step at a particular time point during the displacement of the robot is saved for both signals. The median (μ) and standard deviation (σ) from the particles set are obtained and a random normal distribution is generated based on the values of μ and σ. The distribution of the particles versus the normal distribution is represented in Fig. 24.

Fig. 24(a) shows the percentage of the particles provided by the particle filter using the signal of one of the RF receivers. The similarities of the distribution with the normal distribution (Gaussian) are clearly evident. The same result is obtained in the case of the distribution of the particles using the second RF signal with the 180 degree phase delay (Fig. 24(b)).

From the aforementioned analysis, we can conclude that the

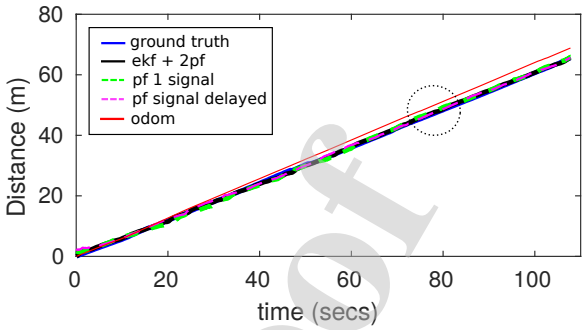

(a) Estimated position comparison using different methods

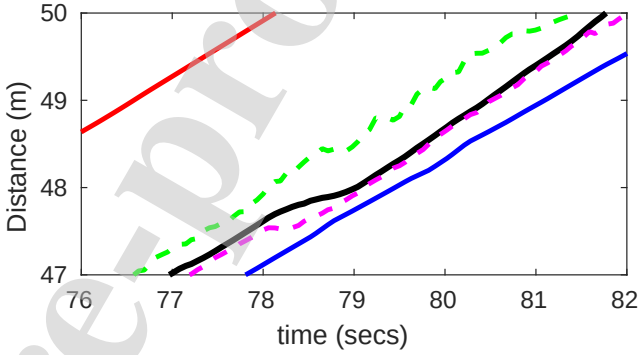

(b) Position detail of the area enclosed by the dotted circle

Fig. 23. Estimated position of the vehicle during its displacement along the pipe: (a) Comparison between the EKF method using both RF signals (black), particle filter using one signal (green and purple dashed line), odometry method (red) and ground truth (blue). (b) Detail of changes in the vehicle position over time corresponding to the enclosed area. The estimated position provided by the EKF (black) closely follows the real position.

assumption of a Gaussian distribution is tenable and therefore the feasibility of the EKF is demonstrated.

VIII. Practical Approach and Lessons Learned

In order to implement the system and obtain an idea about its practicability, we have summarized the important aspects as follows:

- The technique is non-intrusive and does not require environment modifications, only one RF transmitter and one receiver being needed for the simplest setup.
- As a standing wave pattern, the fadings are periodic, repeatable and predictable, and hence, they are suitable for localization.
- The fadings period is given by the pipe diameter and the interacting modes (determined by the operating frequency). In order to propagate n modes, the operating frequency must be higher than the n_{th} mode cutoff frequency but below the $n_{th}+1$ mode cutoff frequency.
- To obtain periodic fadings two modes must be present (bimodal propagation). When more than two propagating modes are present, every possible pair of modes will create a fading structure with its own characteristic spatial period, giving rise to an intricate available power distribution inside the guide. Even in this case, knowing the shape of the modal fields, careful selection of the

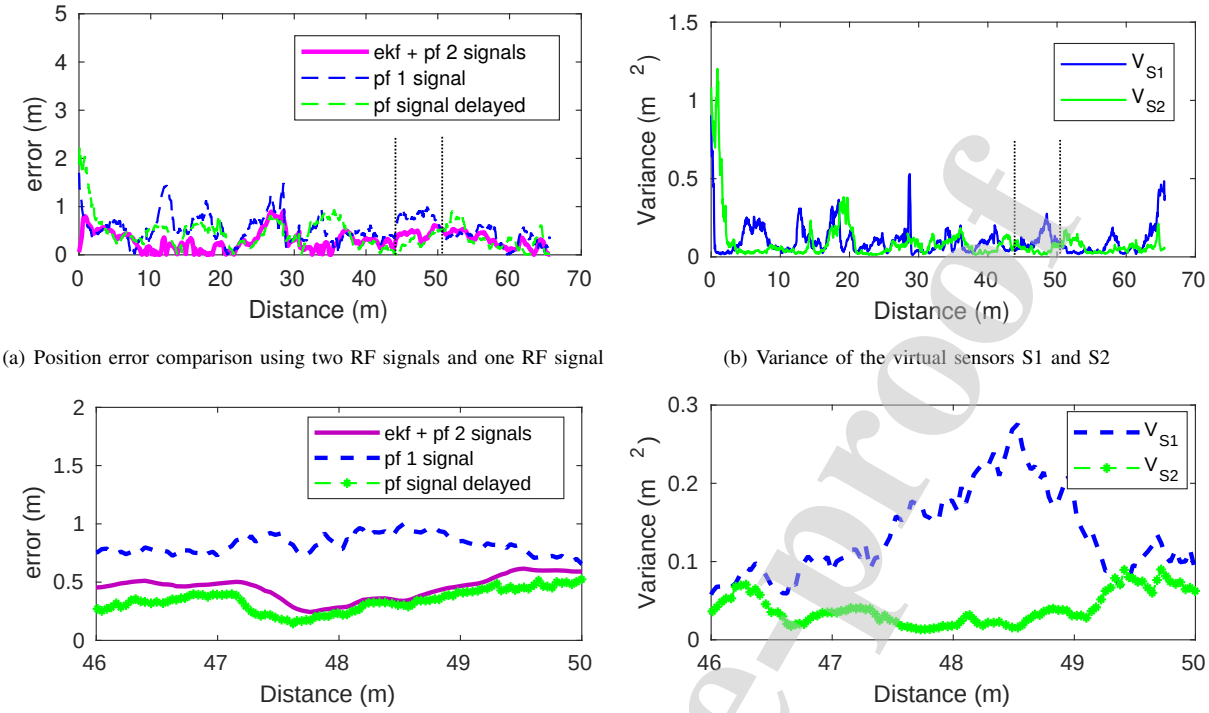

(a) Position error comparison using two RF signals and one RF signal

(b) Variance of the virtual sensors S1 and S2

(c) Position errors, detail corresponding to the enclosed area

(d) Variances, detail corresponding to the enclosed area

Fig. 22. EKF localization method results using two RF signals during the displacement of the robot along the pipe: (a) Position error comparison using the proposed method and the particle filter-based method using one single RF signal. (b) Variance representing the uncertainty in the measurement for each virtual sensor. (c) and (d) Detail of both position errors and variances corresponding to the dotted enclosed area. The final position error is influenced by the best of both virtual sensors in terms of uncertainty. The data from test 3 of Fig. 21 has been used for the comparison with the method using one RF signal.

transmitter and receiver antenna position and orientation in the pipe cross-section can lead to a system that, in fact, operates as if only two modes were present, minimizing the coupling to the unwanted modes on the transmission and/or reception side.

- From Table III, it can be seen that for pipes ranging from 0.15 to 6 m in diameter, the corresponding working frequency varies from around 40 MHz to 2.4 GHz, in order to obtain fadings with a mean period from 0.23 to 30.4 m. Commercial devices that work at the aforementioned frequencies are available at relatively low cost.
- The theoretical analysis presented in this work is limited to pipes that are straight and metallic, these having electrical continuity and uniform cross-section. Although this seems a substantial limitation, it was one of the most common situations found in numerous use-cases. However, the practical analysis presented in Appendix B shows that the localization algorithms would be viable not only in ideal waveguides but also in a wide range of real world pipes with slight to moderate defects and cracks, suffering from local deformations. At last, for different materials such as concrete, the method is still applicable although the suitable frequencies and mode shape considerations would differ, this being beyond the scope of this study (see [26] for an analogy in concrete horseshoe shaped tunnels).
- Inside the pipe, the Faraday cage effect avoids interference from external RF sources, and therefore, the received signal is low in noise.
- The maximum possible length that could be covered is determined by the pipe diameter, material and equipment sensitivity. Metallic pipes have low attenuation rates. In our case study, the Castillonroy pipe was carbon steel with an attenuation rate of less than 9 dB per km, and our low cost receiver has a sensitivity of -105 dBm. This gives us a maximum possible coverage length of several kilometers.
- The discrete and continuous localization algorithms are feasible not only for ground robots but also for aerial robots such as drones.
- The use of two antennas and its correct positioning in the cross section of the pipe allows to improve the accuracy and reliability of both discrete and continuous RF signal based localization methods, by means of exploiting the 180 degree phase difference.
- In the continuous approach, the PF algorithm is more appropriate over the EKF due to the high non-linearity of the RF sensor.
- Localization results from experiments on large-scale pipes can be transferred to small-scale pipes where the RF signal periodicity is also observable (see [20]). In the latter, the expected position error will be significantly smaller (as the fadings period ranges from 0.23 m to 0.4

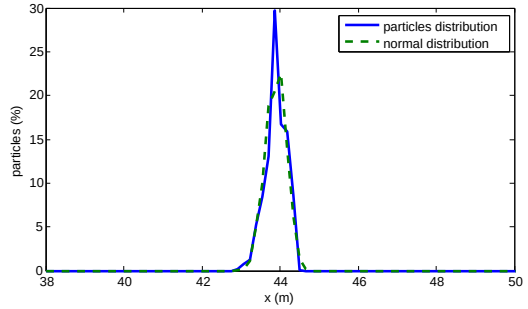

(a) Signal 1

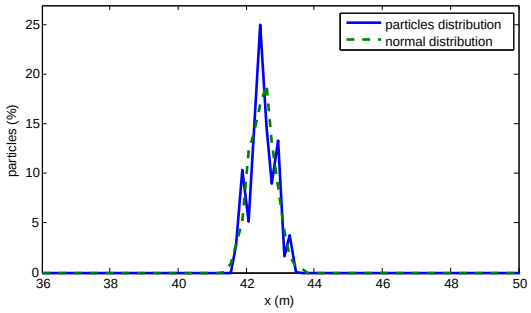

(b) Signal 2

Fig. 24. Particles distribution vs normal distribution after the resampling step. (a) Result using Signal 1. (b) Result using Signal 2 (180 degree phase difference). The two distributions are similar enough to conclude that the assumption of a Gaussian distribution is tenable.

m).

- The position error obtained in this experiment (along 70 m) does not depend on the distance traveled, but on the fidelity of the RF signal with the RF propagation model acting as a RF Map. The error will be remain bounded under acceptable values over the entire length of the pipe in which the effect of periodic fadings appears, i.e, the coverage area which, as mentioned above, extends to several kilometers.

IX. Conclusions

In this paper, we have presented an alternative RF localization method to those existing in the literature (e.g., fingerprint or UWB), which does not require substantial infrastructure deployment or a previously built RF map. Our method is able to localize a robot along a pipe by means of generating and detecting a periodic signal fadings pattern, using just one RF transmitter and one receiver for the simplest setup.

At first, an analysis of the fadings in the longitudinal dimension was performed, followed by determining the influence of the cross-section position of the receiver on the RSSI and relative phase of the fadings. Based on the distribution of the electric field of the interacting modes, the pipe was virtually divided into two halves (vertically or horizontally). Empirical results in a real pipe environment show that depending on the chosen setup, the fadings corresponding to each sector are in phase or present a relative phase difference of about 180 degrees (i.e. a maximum in one signal matching a minimum in the other).

Two approaches for localization, discrete and continuous, have been detailed. The discrete method is based on counting the fadings (maxima and minima) while traversing them, resulting in a sort of RF-odometry. Compared to our previous work, and derived from the transversal fadings analysis in this study, the resolution has been improved by exploiting the 180 degrees phase difference by means of adding two more triggers, corresponding to the crossing points of both signals. In this way, the localization resolution is improved to a quarter of the period of the fadings, this being determined by the pipe's diameter and the operating frequency.

As a step beyond the discrete localization, a continuous localization algorithm has been implemented to estimate the robot displacement along the pipe, using the theoretical fadings model as an RF map. The first of them is based on particle filters and its validity with experimental results was presented in a previous study. Building on that work, the feasibility of using different types of robotic platforms has been confirmed by using an IMU during the prediction step of the particle filter-based method. Apart from that, the applicability of the EKF algorithm using the fadings signal and an RF map has been studied and compared to the particle filter solution. Finally, a new strategy for continuous localization taking advantage of using two RF receivers in order to obtain the 180 phase difference has been developed. This approach consists on fusing the information that comes from two particle filters working with their RF signal and RF map, with an EKF algorithm. The result of a coherence analysis demonstrates the validity of the proposed solution.

All the aforementioned methods have been tested and validated with experiments in a real pipe scenario. The reliability of the discrete localization methods has been proven for in-pipe longitudinal localization. Moreover, the continuous localization using two signals yields better results in terms of error, demonstrating the ability to localize the robot at all times during its displacement along the pipe. Although both methods provide good results, the PF algorithm is more appropriate due to the high non-linearity of the RF sensor.

The RF approach presented in this paper in all its forms overcomes the lack of features that is one of the main difficulties in robot localization in this type of environment. In addition, there is no need for a previously known map and required modifications of infrastructure are minimal, only an RF transceiver placed at the beginning of the pipe being needed to cover several kilometers.

References

[1] E. Siqueira, S. Botelho, R. Azzolin, and V. Oliveira, "A review about robotic inspection considering the locomotion systems and odometry," in *IECON 2016 - 42nd Annual Conference of the IEEE Industrial Electronics Society*, Oct 2016, pp. 571–576.

[2] L. Guan, Y. Gao, H. Liu, W. An, and A. Noureldin, "A review on small-diameter pipeline inspection gauge localization techniques: Problems, methods and challenges," in *2019 International Conference on Communications, Signal Processing, and their Applications (ICCSPA)*, March 2019, pp. 1–6.

[3] H. Sahli and N. El-Sheimy, "A novel method to enhance pipeline trajectory determination using pipeline junctions," *Sensors*, vol. 16, p. 567, 04 2016.

[4] L. Guan, X. Cong, Y. Sun, Y. Gao, U. Iqbal, and A. Noureldin, "Enhanced mems sins aided pipeline surveying system by pipeline junction detection in small diameter pipeline," *IFAC-PapersOnLine*, vol. 50, pp. 3560–3565, 07 2017.

[5] W. Al-Masri, M. Abdel-Hafez, and M. Jaradat, "Inertial navigation system of pipeline inspection gauge," *IEEE Transactions on Control Systems Technology*, vol. PP, pp. 1–8, 11 2018.

[6] P. Hansen, H. Alismail, P. Rander, and B. Browning, "Monocular visual odometry for robot localization in LNG pipes," in *Robotics and Automation (ICRA), 2011 IEEE International Conference on*, May 2011, pp. 3111–3116.

[7] P. Hansen, H. Alismail, B. Browning, and P. Rander, "Stereo visual odometry for pipe mapping," in *2011 IEEE/RSJ International Conference on Intelligent Robots and Systems*, Sep. 2011, pp. 4020–4025.

[8] P. Hansen, H. Alismail, P. Rander, and B. Browning, "Visual mapping for natural gas pipe inspection," *The International Journal of Robotics Research*, vol. 34, no. 4-5, pp. 532–558, 2015. [Online]. Available: https://doi.org/10.1177/0278364914550133

[9] D. Alejo, F. Caballero, and L. Merino, "RGBD-based robot localization in sewer networks," in *Intelligent Robots and Systems (IROS), 2017 IEEE/RSJ International Conference on*, 09 2017, pp. 4070–4076.

[10] D. Tardioli, L. Riazuelo, D. Sicignano, C. Rizzo, F. Lera, J. L. Villarroel, and L. Montano, "Ground robotics in tunnels: Keys and lessons learned after 10 years of research and experiments," *J. Field Robotics*, vol. 36, pp. 1074–1101, 2019.

[11] D. Zhao and W. Whittaker, "High precision in-pipe robot localization with reciprocal sensor fusion," *CoRR*, vol. abs/2002.12408, 2020. [Online]. Available: https://arxiv.org/abs/2002.12408

[12] T. Ozaslan, S. Shen, Y. Mulgaonkar, N. Michael, and V. Kumar, "Inspection of penstocks and featureless tunnel-like environments using micro UAVs." in *Field and Service Robotics.*, ser. Springer Tracts in Advanced Robotics. Springer, Cham, 2015, no. 105, pp. 123–136.

[13] T. Ozaslan, G. Loianno, J. Keller, C. J. Taylor, V. Kumar, J. M. Wozencraft, and T. Hood, "Autonomous navigation and mapping for inspection of penstocks and tunnels with MAVs," *IEEE Robotics and Automation Letters*, vol. 2, no. 3, pp. 1740–1747, July 2017.

[14] A. C. Murtra and J. M. M. Tur, "Imu and cable encoder data fusion for in-pipe mobile robot localization," in *2013 IEEE Conference on Technologies for Practical Robot Applications (TePRA)*, April 2013, pp. 1–6.

[15] J. Torres-Solis and T. H. Falk, "A review of indoor localization technologies : towards navigational assistance for topographical disorientation," in *Ambient Intelligence*, 2017.

[16] A. Alarifi, A. S. Al-Salman, M. Alsaleh, A. Alnafessah, S. Alhadhrami, M. A. Al-Ammar, and H. S. Al-Khalifa, "Ultra wideband indoor positioning technologies: Analysis and recent advances ," in *Sensors*, 2016.

[17] Z. Daixian and Y. Kechu, "Particle filter localization in underground mines using uwb ranging," in *2011 Fourth International Conference on Intelligent Computation Technology and Automation*, vol. 2, March 2011, pp. 645–648.

[18] D. Wu, D. Chatzigeorgiou, K. Youcef-Toumi, and R. Ben-Mansour, "Node localization in robotic sensor networks for pipeline inspection," *IEEE Transactions on Industrial Informatics*, vol. 12, no. 2, pp. 809–819, April 2016.

[19] K. Ma, M. M. Schirru, A. H. Zahraee, R. Dwyer-Joyce, J. Boxall, T. J. Dodd, R. Collins, and S. R. Anderson, "Robot mapping and localisation in metal water pipes using hydrophone induced vibration and map alignment by dynamic time warping," in *2017 IEEE International Conference on Robotics and Automation (ICRA)*, May 2017, pp. 2548–2553.

[20] C. Rizzo, V. Kumar, F. Lera, and J. Villarroel, "RF odometry for localization in pipes based on periodic signal fadings," in *Intelligent Robots and Systems (IROS), 2014 IEEE/RSJ International Conference on*, Sep 2014.

[21] T. Seco, C. Rizzo, J. Espelosín, and J. L. Villarroel, "A Robot Localization System based on RF Fadings using Particle Filters inside Pipes," in *2016 International Conference on Autonomous Robot Systems and Competitions (ICARSC)*, May 2016, pp. 28–34.

[22] C. Rizzo, "Propagation, localization and navigation in tunnel-like environments," Ph.D. dissertation, University of Zaragoza, July 2015.

[23] M. Lazaro and J. Castellanos, "Localization of probabilistic robot formations in SLAM," in *Robotics and Automation (ICRA), 2010 IEEE International Conference on*, May 2010, pp. 3179–3184.

[24] S. Thrun, W. Burgard, and D. Fox, *Probabilistic Robotics (Intelligent Robotics and Autonomous Agents)*. The MIT Press, 2005.

[25] E. Hong and J. Lim, "Visual-inertial odometry with robust initialization and online scale estimation," *Sensors*, vol. 18, p. 4287, 12 2018.

[26] C. Rizzo, F. Lera, and J. L. Villarroel, "3-D fadings structure analysis in straight tunnels toward communication, localization, and navigation," *IEEE Transactions on Antennas and Propagation*, vol. 67, no. 9, pp. 6123–6137, Sep. 2019.

[27] D. Pozar, *Microwave Engineering*, 3rd ed. John Wiley & Sons, 2005.

[28] C. Balanis, *Advanced Engineering Electromagnetics*. John Wiley & Sons, 1989.

[29] C. S. Lee, S. W. Lee, and S. L. Chuang, "Plot of modal field distribution in rectangular and circular waveguides," *Microwave Theory and Techniques, IEEE Transactions on*, vol. 33, no. 3, pp. 271–274, Mar 1985.

[30] C. Balanis, *Antenna Theory: Analysis and Design, 4th Edition*. Wiley, 2016.

[31] C. W. Chuang and P. H. Pathak, "Ray analysis of modal reflection for three-dimensional open-ended waveguides," *IEEE Transactions on Antennas and Propagation*, vol. 37, no. 3, pp. 339–346, March 1989.

[32] S. P. Yeo and S. G. Teo, "Thick eccentric circular iris in circular waveguide," *IEEE Transactions on Microwave Theory and Techniques*, vol. 46, no. 8, pp. 1177–1180, Aug 1998.

[33] M. Miyagi, K. Harada, and S. Kawakami, "Wave propagation and attenuation in the general class of circular hollow waveguides with uniform curvature," *IEEE Transactions on Microwave Theory and Techniques*, vol. 32, no. 5, pp. 513–521, May 1984.

[34] K. Abbasi, S. Ito, H. Hashizume, and K. Yuki, "Evaluation of circumferential crack location in pipes by electromagnetic waves," *Studies in Applied Electromagnetics and Mechanics*, vol. 28, pp. 117–124, 2007, cited By 2.

[35] G. Brooker, R. Hennessey, C. Lobsey, M. Bishop, and E. Widzyk-Capehart, "Seeing through dust and water vapor: Millimeter wave radar sensors for mining applications," *Journal of Field Robotics*, vol. 24, no. 7, pp. 527–557, 2007. [Online]. Available: https://doi.org/10.1002/rob.20166

APPENDIX A
DETAILS ON RF PROPAGATION IN PIPES

A circular cross-section metallic pipe behaves as a cylindrical waveguide for RF signals. Electromagnetic wave propagation inside the guide is strongly frequency dependent. This is a classical problem. Further details and fully worked solutions can be found in Chapter 3 of [27] and Chapter 9 of [28].

We consider the pipe to be an infinitely long air-filled hollow cylinder, with free space permittivity ϵ_0 and permeability μ_0, and that it has metallic walls of electrical conductivity σ and magnetic permeability μ, with internal radius a. The usual approach involves the solution of the electromagnetic wave equation in the frequency domain, for a fixed frequency, f or $\omega = 2\pi f$, to obtain complex-valued electric and magnetic field expressions depending only on the space variables, for example $\vec{E}(\vec{r})$. The time- and space-dependent field can be obtained, if needed, as $\vec{E}(\vec{r},t) = Real(\vec{E}(\vec{r})e^{j\omega t})$. In the following, all magnitude amplitudes are rms values.

A. Modal fields in cylindrical waveguides

The electromagnetic fields inside a cylindrical waveguide are best described in cylindrical coordinates (ρ,ϕ,x) to take advantage of the geometrical symmetry. Notice that we use x instead of z as the axial coordinate for the longitudinal position of the robots in the pipe. Applying the electromagnetic boundary conditions at the metallic wall, considered a good conductor, there are infinite solutions to the frequency domain wave equation, with their associated field configurations. These symmetry-adapted solutions are customarily called modes, and are classified as Transverse Electric (TE, those with no electric field component in the longitudinal direction) or Transverse Magnetic (TM, those with no magnetic field component in the longitudinal direction). These modes are further indexed with two integer subscripts (m=0,1,2,3... ; n=1,2,3...) that account for the mode structure across the ρ and ϕ dimensions. Each TE_{mn} or TM_{mn} mode describes a geometrical arrangement of the electromagnetic fields in the guide cross-section. Fig. 25 shows, as an example, the electric

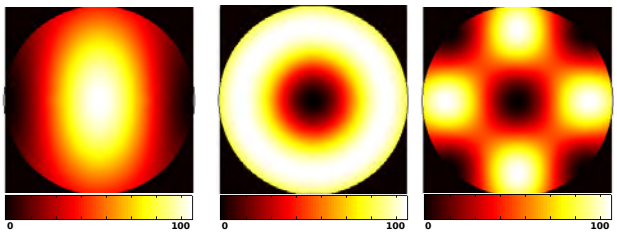

(a) TE_{11} (b) TM_{01} (c) TE_{21}

Fig. 25. Normalized intensity (arbitrary units) for the first three propagating modes inside a metallic cylindrical waveguide

field distribution of the first three modes. See [27], [28] or [29] for plotted examples of higher-order modes.

Waveguides are high-pass frequency-selective devices. For each mode, there is a geometry-dependent cutoff frequency, f_c. RF fields of frequency f can propagate along the guide only in modes with $f_c < f$. For an air-filled cylindrical pipe of radius a, the cutoff frequency for TM modes is given by:

$$f_c^{mn} = \chi_{mn} \frac{c}{2\pi a} \tag{19}$$

and for TE modes by:

$$f_c^{mn} = \chi'_{mn} \frac{c}{2\pi a} \tag{20}$$

where $c = 1/\sqrt{\epsilon_0 \mu_0}$ is the free space speed of light, χ_{mn} is the n-th zero of the Bessel function J_m of the first kind and χ'_{mn} is the n-th zero of J'_m, the derivative of the Bessel function J_m of the first kind. The mode with the lowest cutoff frequency, called the dominant mode, is TE_{11} with χ'_{11}=1.8412. No RF propagation is possible in the circular guide for frequencies below this value. The next three cutoff frequencies correspond to TM_{01} with χ_{01}=2.4049, TE_{21} with χ'_{21}=3.0542 and the degenerate TE_{01} and TM_{11} modes with χ'_{01}=χ_{11}=3.8318.

In free space λ_0, the wavelength of an RF wave of frequency f, and its associated free space wavenumber β_0 are governed by the simple expression:

$$\lambda_0 = \frac{c}{f} = \frac{2\pi}{\beta_0} \tag{21}$$

In waveguides, the situation is more complex and, for a given frequency f, each propagating mode - with $f_c < f$ - has its own guide wavelength λ_{mn} and associated guide wavenumbers along the x (β_{mn}) and ρ (β_ρ^{mn}) dimensions:

$$\lambda_{mn} = \frac{2\pi}{\beta_{mn}} = \frac{\lambda_0}{\sqrt{1 - \left(\frac{f_c^{mn}}{f}\right)^2}} \tag{22}$$

with

$$(\beta_\rho^{mn})^2 = (\beta_0)^2 - (\beta_{mn})^2 \tag{23}$$

The shape of the electromagnetic fields is usually described by the so-called modal fields, which are general forms of the particular solutions of the wave equation for each mode. The components of the electric modal fields for TM modes are:

$$e_\rho^{mn} = \frac{-j\omega\mu_0 m}{(\beta_\rho^{mn})^2 \rho} J_m(\beta_\rho^{mn}\rho)(A\cos m\phi - B\sin m\phi) \tag{24}$$

$$e_\phi^{mn} = \frac{j\omega\mu_0}{\beta_\rho^{mn}} J'_m(\beta_\rho^{mn}\rho)(A\sin m\phi + B\cos m\phi) \tag{25}$$

$$e_x^{mn} = 0 \tag{26}$$

and the components of the modal fields for TE modes are:

$$e_\rho^{mn} = \frac{-j\beta_{mn}}{\beta_\rho^{mn}} J'_m(\beta_\rho^{mn}\rho)(A\sin m\phi + B\cos m\phi) \tag{27}$$

$$e_\phi^{mn} = \frac{-j\beta_x^{mn} m}{(\beta_\rho^{mn})^2 \rho} J_m(\beta_\rho^{mn}\rho)(A\cos m\phi - B\sin m\phi) \tag{28}$$

$$e_x^{mn} = J_m(\beta_\rho^{mn}\rho)(A\cos m\phi - B\sin m\phi) \tag{29}$$

The total modal electric field is then:

$$\vec{e}_{mn} = (e_\rho^{mn}\hat{\rho} + e_\phi^{mn}\hat{\phi} + e_x^{mn}\hat{x}) \tag{30}$$

Similar equations can be obtained for the magnetic field components, h_ρ^{mn}, h_ϕ^{mn} and h_x^{mn}.

There are two arbitrary amplitude constants, A and B, in the above expressions. These constants control the amplitude of the independent $\sin n\phi$ and $\cos n\phi$ terms. This is due to the azimuthal symmetry of the cylindrical waveguide, and in fact, one can consider the two extreme cases (A=1, B=0 and viceversa) as two linearly independent degenerate modes orthogonal to one another (with the same cutoff frequency, wavelength, etc.). In a real situation, the amplitude of each mode present in the guide will depend on the direction of the excitation field. An equivalent viewpoint is to consider A and B to be parameters for controlling the azimuthal rotation of the corresponding modal field.

The time-average power flow associated with each modal field can be calculated as a surface integral over the guide cross-section, S_0:

$$P_{mn} = \int_{S_0} Real(\vec{e}_{mn} \times \vec{h}^*_{nm})\, \hat{x}\, ds \tag{31}$$

where the superscript * represents complex conjugation.

Losses arising from the finite conductivity of the pipe wall are included through the attenuation term α_{mn} in the guide propagation constant of each mode $\gamma_{mn} = \alpha_{mn} + j\beta_{mn}$. For TE modes,

$$\alpha_{mn} = \frac{\lambda_{mn} R_s}{a\,\eta_0} \times \left[\left(\frac{f_c^{mn}}{f}\right)^2 + \frac{m^2}{\chi'^2_{mn} - m^2}\right] \tag{32}$$

and for TM modes:

$$\alpha_{mn} = \frac{\lambda_{mn} R_s}{a\,\eta_0} \tag{33}$$

where $R_s = \sqrt{\omega\mu/2\sigma}$ is the surface impedance of the metallic conductor and $\eta_0 = \sqrt{\mu_0/\epsilon_0}$ is the free space characteristic impedance.

B. Antenna coupling to modal fields

An RF source (usually an antenna) at a given frequency f inside a pipe generates a complex RF field that is a superposition of many different modes with different amplitudes. At short distances from the antenna (a single free space wavelength is enough), only the propagating modes - those with $fc < f$ - will be present.

To calculate the power coupled to each mode from the excitation source, we follow a standard microwave procedure as described in Chapter 4 of [27]. The electric field of a forward traveling wave in the pipe can be expressed as a linear combination of the modes supported by the guide:

$$\vec{E} = \sum_{mn} A^+_{mn} \vec{e}_{mn} e^{-\gamma_{mn} x} \tag{34}$$

with the summation extending only to the TE and TM propagating modes allowed for the operating frequency and pipe radius. There, A^+_{mn} is the complex rms amplitude at $x = 0$ of the

corresponding mn mode electric field. The propagation term is $e^{-\gamma_{mn}x} = e^{-j\beta_{mn}x}\, e^{-\alpha_{mn}x}$ where $\beta_{mn}x = 2\pi x/\lambda_{mn}$ represents the accumulated phase delay and $e^{-\alpha_{mn}x}$ is the attenuation suffered by the modal electric field after traveling a distance x along the guide.

In this work, we have used electrically short (that is, with length $l < \lambda_0/10$), thin linear antennas for RF excitation and detection, always contained in the pipe cross-section plane. We set $x = 0$ in the transmitting antenna (tx) position. The current flowing in these antennas can be approximated well as a triangular distribution with a maximum I_0 at the antenna feeding point and vanishing at the antenna ends. These antennas radiate linearly polarized fields; see [30] for further details. Their radiation resistance is $R_r = 20\pi^2(l/\lambda_0)^2$ and the total radiated power is:

$$P_{rad} = I_0^2 R_r \tag{35}$$

An inversion procedure allows for the determination of the modal amplitudes excited by the antenna:

$$A_{mn}^{+} = -\frac{1}{2P_{mn}} \int_{ant} \vec{e}_{mn}(r')I(r')d\vec{r}' \tag{36}$$

Here, the variable r' represents the position in the transmitting antenna and the line integral is calculated along its length. To maximize (minimize) the coupling to a given mode from the transmitting antenna, the antenna position in the pipe cross-section has to be chosen to be at a place where the modal field intensity is maximum (minimum, ideally null) and its orientation has to be ideally parallel (orthogonal) to the modal field direction there. Moreover, the modal field symmetry can be used to minimize coupling choosing a place and orientation where the aforementioned integral goes to zero because the contribution of one half cancels out the contribution of the other half.

On the other hand, from reciprocity, when an electric field $\vec{E}$ impinges on an electrically short receiving (rx) antenna it produces an open-circuit voltage:

$$V_{oc} = -\frac{1}{I_0} \int_{ant} \vec{E}(r')I(r')d\vec{r}' \tag{37}$$

Thus, recalling that $\vec{E}$ is a linear combination of the propagating modes, as shown in Eq. (34), the same geometrical considerations as above are valid to minimize (maximize) the coupling of a given $\vec{e}_{mn}$ modal field component present on $\vec{E}$ to the receiving antenna.

The power that the antenna delivers to a matched load is:

$$P_L = \frac{V_{oc}^2}{4R_r} \tag{38}$$

The actual power delivered is usually lower due to impedance mismatch and ohmic losses in the antenna and wiring.

The procedure to estimate the power received in an antenna at position rx from a transmitting antenna at position tx - remembering that $x = 0$ there - is as follows, assuming that both antennas are electrically short. Knowing the radiated power of the transmitting antenna, I_0 is calculated from Eq. (38). Then, the modal amplitudes can be obtained using Eq. (36) and, from these, the electric field on the receiving antenna position can be calculated using Eq. (34). Then, Eqs. (37) and (38) give the received power.

APPENDIX B
FADINGS IN NON-IDEAL PIPES

The previous analysis applies to ideal cylindrical waveguides, where ideal means that the waveguide is straight, its length is assumed infinite, its internal diameter is constant, the inner surface is smooth without cracks and there are not obstacles or obstructions inside. This is not the case in real world waveguides specifically designed for communications, nor in metallic pipes built for different purposes, where defects arising from non-idealities will exist. When

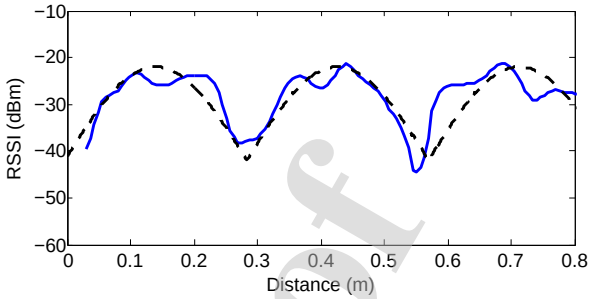

(a) Received RSSI. The dashed line represents the theoretical fadings in an ideal pipe, and the blue lines the recorded received power.

(b) Corrugated aluminum pipe

(c) Motorized moving receiver

(d) Hokuyo LiDAR for ground-truth

(e) Transmitting antenna (*f=2650 MHz*)

Fig. 26. Corrugated pipe experimental setup. The transmitter was placed in the right extreme of the pipe, and a small robot was displaced along the straight part. Both obstacles (robot and LiDAR) are obstructing a substantial part of the pipe cross section.

a propagating mode reaches a defect, a given fraction of the power that it carries will be scattered and coupled to each other possible propagating mode, traveling forward and also reflected backwards. Moreover, it will locally excite non-propagating modes noticeable only in close proximity to the defect. The consequence of this scattering is twofold: an increase of the attenuation constant with respect to the ideal waveguide, and the interference of the forward and backwards propagating modes, that adds a standing wave contribution to the RF available power distribution in the guide. In this work we have proposed to use the periodic spatial fading structure arising from multimodal forward propagation for in-pipe 1D localization of a robot traveling along a pipe. Thus we must check if this localization method is still valid taking into account the unwanted effects coming from non-idealities present in real world pipes.

The frequency selected for our practical application limits the propagating modes present inside the pipe to the first three, at most, namely the TE_{11}, TM_{01} and TE_{21} modes. In fact, we placed the transmitting antenna in a way that minimized (ideally, nulled) the TM_{01} amplitude. Thus, we must check how defects scatter these three modes.

- Pipe length: first of all, the pipe length is always finite. The power reflection coefficient in a pipe flanged open ends can be estimated numerically following [31]. For symmetry considerations, a given TX_{mn} mode can couple only to TX_{mp} modes, and thus no cross-modal coupling is induced by the pipe

ends. For the experimental scenario described in this paper the power reflection coefficients for the three propagating modes are calculated as $1.6x10^{-5}$, $2.5x10^{-3}$ and $6.2x10^{-2}$. The standing wave component added is negligible for the first two and only creates a weak ripple for the third one that can be easily filtered out during data collection.

- Presence of obstacles: the presence of obstacles without cylindrical symmetry in the general case will produce both reflections and intermodal coupling. In the experimental work presented in [20], given the small size of the pipe, the LiDAR used for localization at the pipe end represents an obstacle occupying around a quarter of the cross section, see Fig.26 . The emitter setup and the receiver robotic chariot are also of non-negligible size when compared to the pipe diameter. Nevertheless, the measured fadings fit quite well the theory, both in spatial period and shape. In [32] a method to compute the effect of a narrowing of the pipe is given. In Table 1 therein, the scattering power coefficients from the dominant TE_{11} mode to all the possible forward and backwards propagating modes are shown for a waveguide that supports the first three modes with an eccentric narrowing to 55% of its section for a length of half its radius. The biggest coefficient is 0.12, all the others are below 0.052 and thus the scattering in the collapsed region will add only a modest standing wave component to the RF field.
- Presence of curved sections: another concern comes from the presence of curved sections along the pipe. As explained in [33], the propagation constant of the modes is barely modified if the curvature radius of the bent sector is much bigger than the pipe radius, as is our case, and coupling among modes is relevant only from TM_{0q} to TE_{0q}, not possible within our working frequency.
- Cracks: a crack in the metallic pipe will distort locally the currents that support wave propagation and thus will also give rise to scattering. This is indeed the basis for on-site RF use as non-destructive crack location system in pipes, see for example [34]. The experimental results therein show that a power reflection coefficient below 0.005 appears for an intentionally semicircumferential cut in a pipe. This small reflection is still useful for crack location with the adequate high sensitivity instrumentation, but has negligible effect on the fading pattern of our interest.
- Non-smooth surfaces: we have also performed several experiments in corrugated aluminium flexible pipes, with non-smooth inner surfaces, and there also the fading period and shape fitted quite well with the model (see Fig. 26).
- Darkness, water vapor, dust and smoke: RF propagation is not affected by lightning conditions. Dust, water vapor and smoke are small particle aerosols that will not affect RF propagation at frequencies below 10-100 GHz, which is an advantage over LiDARs and cameras [35].
- Remaining liquid in the pipe: Scattered water or oil puddles will not affect the RF propagation inside the pipe. If however the pipe is not fully empty and a shallow liquid depth is present along all its length, this geometry change will break the circumferential symmetry and affect the modal wavelengths and thus the fading period. We have performed FEM simulations in a 4 m diameter pipe with a remaining depth of 5 and 15 cm of stream water. The results show that the fading period of the TE_{11} and TE_{21} horizontally polarized modes interference changes by 0.3 and 1.2 percent respectively, within the experimental uncertainty. The effect of similar depths of crude oil is even lower.

All these results support that the proposed localization scheme would be viable not only in ideal waveguides but also in a wide range of real world pipes with slight to moderate defects and cracks, suffering from local deformations and/or obstacles present.

At last, in Table III we have summarized some results of environments in which we have analyzed these fadings, such as the penstock pipe of the Allatoona Dam in Atlanta (Georgia, USA), and common case studies in the literature.

TABLE III
EXPERIMENTS WITH DIFFERENT PIPES

	Small pipes	Gasoduct	Castillon Dam pipe	Allatoona Dam penstock pipe
Diameter [m]	0.15	0.40	4	6
f_{c2} [MHz]	1500	574	57	**38**
f_{c3} [MHz]	1900	729	73	48
f_{c4} [MHz]	**2400**	914	91	60
Bimodal fading period [m]	0.38-0.76	1.01-2.02	10.1-20.2	15.2-**30.4**
Trimodal fading period [m]	**0.23**-0.40	0.61-1.08	6.15-10.8	9.23-16.2

It can be seen that ranging from 0.15 to 6 m in diameter, the corresponding working frequency varies from around 40 MHz to 2.4 GHz, in order to obtain fadings with a mean period from 0.23 to 30.4 m (values highlighted in bold). We have selected frequencies of about 1% above/below the cutoff frequency of the second/third modes for bimodal propagation, and the equivalent with the third/fourth modes for trimodal propagation, in order to explore the whole range.

Commercial devices to work at the aforementioned frequencies are available at relatively low cost.

ROBOT_2019_300

HIGHLIGHTS

- By choosing an appropriate frequency, strictly periodic RF spatial fadings appear in pipes.
- RF fadings period scale with the pipe's diameter and operating frequency.
- Periodic RF spatial fadings can be used for both discrete and continuous localization estimation in pipes.
- RF localization approach works despite humidity, darkness, low lightning, obstacles, deformations of noticeable size compared to the pipes diameter.
- Localization error decreases in continuous approach compared to a discrete approach.

Author Biographies

Carlos Rizzo received his B.Sc. degree (with Honors) in Electronic Engineering in 2009, and the M.Sc. degree and Ph.D. (with Honors) in Computer Science from University of Zaragoza in 2011 and 2015 respectively. His research interests are in wireless propagation models and protocols, and its applications in communications-aware robotics, specifically for robot localization and navigation under connectivity constraints.

Teresa Seco received her B.Sc. degree in Industrial Engineering (Electronics, Computing and Control specialization) and M.Sc. degree in System and Computer Engineering from University of Zaragoza, Spain, in 1997 and 2011 respectively. She is completing her Ph.D. in System and Computer Engineering from University of Zaragoza. Since 1998 she is working at Instituto Tecnológico de Aragón currently belonging to its robotics group where she develops innovative solutions related to mobile robotics and industrial applications. Her research interests include robot localization in confined areas with communication constrains.

Jesus Espelosín received his B.Sc. degree in Electronic and Automatic Engineering, and the Ph.D. in Physics and Computer Engineering from University of La Laguna, Spain, in 2008 and 2013 respectively. Since 2013 he is working at Instituto Tecnológico de Aragón currently belonging to its robotics group where he develops innovative solutions related to mobile robotics and industrial applications. His research interests include path planning on dynamic scenarios, robot localization in challenging environments and robot perception.

Francisco Lera received the M.Sc. and the Ph.D. degrees in physics from the University of Zaragoza in 1985 and 1990, respectively. He was initially with the Instituto de Ciencia de Materiales de Aragón, CSIC-University of Zaragoza, where he worked on applied superconductivity and advanced instrumentation. Since 1994, he is Associate Professor of Signal Theory and Communications in the Department of Electronic Engineering and Communications at the University of Zaragoza. Since 2012 he is also member of the Robotics, Perception and Real-Time Group within the Aragon Institute for Engineering Research (I3A). His research is now focused on electromagnetic propagation in complex environments, from theoretical modeling to the application development. Some examples are tunnels, galleries, pipes, mines, snow covered mountain areas and through the earth communications.

José Luis Villarroel received his B.Sc. and Ph.D. degrees in Industrial Engineering from University of Zaragoza in 1985 and 1990. Since then, he has been a Professor of Systems Engineering and Automatic Control, with more than 25 years of experience in Real-Time and Embedded Systems. He is head of the Hostile Environments Techonologies Group (`Grupo de Tecnologías en Entornos hostiles -(GTE)') and member of the Robotics, Perception and Real-Time Group (RoPeRT). His main research interests are in real-time systems, ad-hoc networks, robotics, communication systems in confined environments and application of systems engineering to natural systems. He has participated in a total of 44 research projects (coordinating 16 of them), holding two international patents and one national patent.

Declaration of interests

☑ The authors declare that they have no known competing financial interests or personal relationships that could have appeared to influence the work reported in this paper.

☐ The authors declare the following financial interests/personal relationships which may be considered as potential competing interests:

Carlos Rizzo
April 27, 2019

Teresa Seco
April 27, 2019

Jesús Espelosín
April 27, 2019

Francisco Lera
April 27, 2019

Jose Luís Villarroel
April 27, 2019